Bose-Hubbard models in confining potentials: Inhomogeneous mean-field theory

Ramesh V. Pai[*]

Department of Physics, Goa University, Taleigao Plateau, Goa 403 206, India

Jamshid Moradi Kurdestany[†]

Centre for Condensed Matter Theory, Department of Physics, Indian Institute of Science, Bangalore 560 012, India

K. Sheshadri[‡]

Bagalur, Bangalore North Taluk, India 562 149, India

Rahul Pandit[§]

Centre for Condensed Matter Theory, Department of Physics, Indian Institute of Science, Bangalore 560012, India

We present an extensive study of Mott insulator (MI) and superfluid (SF) shells in Bose-Hubbard (BH) models for bosons in optical lattices with harmonic traps. For this we apply the inhomogeneous mean-field theory developed by Sheshadri *et al.* [Phys. Rev. Lett. **75**, 4075 (1995)]. Our results for the BH model with one type of spinless bosons agree quantitatively with quantum Monte Carlo simulations. Our approach is numerically less intensive than such simulations, so we are able to perform calculations on experimentally realistic, large three-dimensional systems, explore a wide range of parameter values, and make direct contact with a variety of experimental measurements. We also *extend* our inhomogeneous mean-field theory to study BH models with harmonic traps and (a) two species of bosons or (b) spin-1 bosons. With two species of bosons, we obtain rich phase diagrams with a variety of SF and MI phases and associated shells when we include a quadratic confining potential. For the spin-1 BH model, we show, in a representative case, that the system can display alternating shells of polar SF and MI phases, and we make interesting predictions for experiments in such systems.

PACS number(s): 67.85.Bc, 67.85.Fg, 03.75.Mn, 05.30.Jp

I. INTRODUCTION

High-precision experiments on cold atoms, such as spin-polarized ^{87}Rb, in traps have provided powerful methods for the study of quantum phase transitions,[1] e.g., the transition from a superfluid (SF) to a bosonic Mott insulator (MI) in an optical lattice.[2,3] This transition was predicted by mean-field studies[4,5] and obtained in Monte Carlo simulations[6] of the Bose-Hubbard model before it was seen in experiments.[1–3] Recent experiments[7,8] have investigated a heteronuclear degenerate mixture of two bosonic species, e.g., ^{87}Rb and ^{41}K, in a three-dimensional (3D) optical lattice; such mixtures have also been studied theoretically[9–15] by Monte Carlo simulations[16,17] and by bosonic dynamic mean-field theory.[18] Systems of alkali atoms with nuclear spin $I = 3/2$ have hyperfine spin $F = 1$; examples include ^{23}Na, ^{39}K, and ^{87}Rb. These spins are frozen in magnetic traps, so these atoms are treated as spinless bosons; however, in purely optical traps, such spins can form spinor condensates.[19–22] Thus, we consider the following three types of Bose-Hubbard (BH) models: (1) a BH model for spinless interacting bosons of one type; (2) a generalization of the spinless BH model with two types of bosons; and (3) a spin-1 generalization of the spinless BH model with bosons of one type. We study these models by developing extensions of an inhomogeneous mean-field theory,[23] which has been used for the Bose-glass phase in the disordered BH model.

In addition to the optical-lattice potential, a confining potential, which is typically quadratic, is present in all experiments. This inhomogeneous potential leads to inhomogeneities in the phases that are obtained: simulations[24,25] of the Bose-Hubbard model with this confining potential and experiments[26,27] on interacting bosons in optical lattices with a confining potential have both seen alternating shells of SF and MI regions in the single-species, spinless case. We explore such shells via the inhomogeneous mean-field theory, first for single-species, spinless bosons and then for the two-species and spin-1 generalizations mentioned above.

Mean-field theories for the Bose-Hubbard model were first developed for the homogeneous case;[4,5] these theories were then extended to the inhomogeneous case[23] to develop an understanding of the Bose-glass phase in the disordered Bose-Hubbard model. This approach provides a natural framework for understanding alternating SF and MI shells, which are seen in simulations[24,25] and experiments[26,27] on interacting bosons, trapped in a confining potential, and in an optical lattice, and it is equivalent to the inhomogeneous Gutzwiller mean-field theory, which has been applied recently to the evolution of condensate fractions during rapid lattice ramps.[28] Although other groups[29–34] have studied such shell structure theoretically, they have not obtained the quantitative agreement with quantum Monte Carlo (QMC) simulations[24] that we obtain, except in one dimension.[35] Furthermore, our theory yields results in good agreement with a variety of experiments, and it can be extended easily to (a) two species of interacting bosons and (b) the spin-S case, as we show explicitly for $S = 1$. In both these cases, we provide interesting predictions that will, we hope, stimulate new experiments. Our inhomogeneous mean-field calculations can be carried out with experimentally realistic parameters, so we can make direct comparison with experiments. In particular, we obtain in-trap density

distributions of alternating SF and MI shells; these show plateaus in certain regions, which can be understood on the basis of simple geometrical arguments. Furthermore, we obtain the radii of SF and MI shells from in-trap density distributions and demonstrate how the phase diagram of the homogeneous Bose-Hubbard model can be obtained from these radii. We also obtain results that are of direct relevance to recent atomic-clock-shift experiments.[27] With two species of bosons, we obtain phase diagrams in the homogeneous case over a far wider range of parameters than has been reported hitherto. We find rich phase diagram with phases that include ones in which (a) both types of bosons are in SF states, (b) both types of bosons are in MI phases with different or the same densities, and (c) one type of boson is in an SF phase, whereas the other type is in an MI phase. We show that each of these phases appears in shells when we include a quadratic confining potential; we also obtain in-trap density distributions that show plateaux as in the single-species case. In the case of the spin-1 Bose-Hubbard model, we show, in a representative case, that the system can display alternating shells of polar SF (Ref. 22) and MI phases; the latter have integral values for the boson density.

The remaining part of this paper is organized as follows. In Sec. II, we describe (a) the models we use and (b) how we develop an inhomogeneous mean-field theory for them. Section III is devoted to our results; Sec. III A contains the results of our inhomogeneous mean-field theory for the single-species, spinless Bose-Hubbard model; Sec. III B is devoted to the results, for both homogeneous and inhomogeneous cases, for the spinless BH model with two types of bosons; Sec. III C is devoted to our results for the single-species BH model for spin-1 bosons. Section IV contains our conclusions, a comparison of our work with earlier studies in this area, and the experimental implications of our results.

II. MODELS AND INHOMOGENEOUS MEAN-FIELD THEORY

We begin by defining the three Bose-Hubbard models that we study. We then describe inhomogeneous mean-field theories that are well suited for studying the spatial organization of phases in these models with confining potentials.

A. Models

The simplest Bose-Hubbard model describes a single species of spinless bosons in an optical lattice by the following Hamiltonian:

$$\frac{\mathcal{H}}{zt} = -\frac{1}{z}\sum_{\langle i,j\rangle}(a_i^\dagger a_j + \text{H.c.}) + \frac{1}{2}\frac{U}{zt}\sum_i \hat{n}_i(\hat{n}_i - 1)$$
$$- \frac{1}{zt}\sum_i \mu_i \hat{n}_i; \tag{1}$$

here, spinless bosons hop between the z nearest-neighbor pairs of sites $\langle i,j\rangle$ with amplitude t, $a_i^\dagger$, a_i, and $\hat{n}_i \equiv a_i^\dagger a_i$ are, respectively, boson creation, annihilation, and number operators at the sites i of a d-dimensional hypercubic lattice (we study $d = 2$ and 3), U the onsite Hubbard repulsion, $\mu_i \equiv \mu - V_T R_i^2$, μ the uniform chemical potential that controls

the total number of bosons, V_T the strength of the harmonic confining potential, and $R_i^2 \equiv \sum_{n=1}^d X_n^2(i)$, where $X_n(i)$, $1 \leqslant n \leqslant d$, are the Cartesian coordinates of the site i (in $d = 3$, $X_1 = X$, $X_2 = Y$, and $X_3 = Z$); the origin is chosen to be at the center of the lattice. In terms of experimental parameters[1] $\frac{U}{zt} = \frac{\sqrt{8}\pi}{4z}\frac{a_s}{a}\exp(2\sqrt{\frac{V_0}{E_r}})$, where E_r is the recoil energy, V_0 the strength of the lattice potential, a_s (=5.45 nm for ^{87}Rb) the s-wave scattering coefficient, $a = \lambda/2$ the optical-lattice constant, and $\lambda = 825$ nm the wavelength of the laser used to create the optical lattice; typically, $0 \leqslant V_0 \leqslant 22E_r$. We set the scale of energies by using $zt = 1$ in the Bose-Hubbard model (1); for comparisons with experimental systems, we should scale all energies by E_r.

For a mixture with two types of bosons, we use the following Bose-Hubbard Hamiltonian:

$$\frac{\mathcal{H}}{z} = -\frac{t_a}{z}\sum_{\langle i,j\rangle}(a_i^\dagger a_j + \text{H.c.}) - \frac{t_b}{z}\sum_{\langle i,j\rangle}(b_i^\dagger b_j + \text{H.c.})$$
$$+ \frac{1}{2}\frac{U_a}{z}\sum_i \hat{n}_{ai}(\hat{n}_{ai} - 1) + \frac{1}{2}\frac{U_b}{z}\sum_i \hat{n}_{bi}(\hat{n}_{bi} - 1)$$
$$+ \frac{U_{ab}}{z}\sum_i \hat{n}_{ai}\hat{n}_{bi} - \frac{1}{z}\sum_i \mu_{ai}\hat{n}_{ai} - \frac{1}{z}\sum_i \mu_{bi}\hat{n}_{bi}. \tag{2}$$

The first and second terms represent, respectively, the hopping of bosons of types a and b between the nearest-neighbor pairs of sites $\langle i,j\rangle$ with hopping amplitudes t_a and t_b; here, $a_i^\dagger$, a_i, and $\hat{n}_{ai} \equiv a_i^\dagger a_i$ and $b_i^\dagger$, b_i, and $\hat{n}_{bi} \equiv b_i^\dagger b_i$ are, respectively, boson creation, annihilation, and number operators at the sites i of a d-dimensional hypercubic lattice (we study $d = 2$ and 3) for the two bosonic species. For simplicity, we restrict ourselves to the case $t_a = t_b = t$, and, to set the scale of energies, we use $zt = 1$. The third and fourth terms account for the onsite interactions of bosons of a given type, with energies U_a and U_b, respectively, whereas the fifth term, with energy U_{ab}, arises because of the onsite interactions between bosons of types a and b. We have two chemical potential terms: $\mu_{ai} \equiv \mu_a - V_{Ta}R_i^2$ and $\mu_{bi} \equiv \mu_b - V_{Tb}R_i^2$, where μ_a and μ_b are the uniform chemical potentials that control the total number of bosons, of species a and b, respectively, V_{Ta} and V_{Tb} are the strengths of their harmonic confining potentials (we restrict ourselves to the case $V_{Ta} = V_{Tb}$), and $R_i^2 \equiv \sum_{n=1}^d X_n^2(i)$, where $X_n(i)$, $1 \leqslant n \leqslant d$, are the Cartesian coordinates of the site i; the origin is at the center of the lattice.

The spin-1 Bose-Hubbard Hamiltonian[22] that we consider is

$$\frac{\mathcal{H}}{zt} = -\frac{1}{z}\sum_{\langle i,j\rangle,\sigma}(a_{i,\sigma}^\dagger a_{j,\sigma} + \text{H.c.}) + \frac{1}{2}\frac{U_0}{zt}\sum_i \hat{n}_i(\hat{n}_i - 1)$$
$$+ \frac{1}{2}\frac{U_2}{zt}\sum_i (\vec{F}_i^2 - 2\hat{n}_i) - \frac{1}{zt}\sum_i \mu_i \hat{n}_i. \tag{3}$$

Here, spin-1 bosons can occupy the sites i of a d-dimensional, hypercubic lattice and hop between the z nearest-neighbor pairs of sites $\langle i,j\rangle$ with amplitude t, σ is the spin index that can be $1, 0, -1$, $a_{i,\sigma}^\dagger$ and $a_{i,\sigma}$ are, respectively, site- and spin-dependent boson creation and annihilation operators, and the number operator $\hat{n}_{i\sigma} \equiv a_{i,\sigma}^\dagger a_{i,\sigma}$; the total number operator at

site i is $\hat{n}_i \equiv \sum_\sigma \hat{n}_{i,\sigma}$, and $\vec{F}_i = \sum_{\sigma,\sigma'} a^\dagger_{i,\sigma} \vec{F}_{\sigma,\sigma'} a_{i,\sigma'}$ with $\vec{F}_{\sigma,\sigma'}$ standard spin-1 matrices. The model (3) includes, in addition to the onsite repulsion U_0, an energy U_2 for nonzero spin configurations on a site. Such a spin-dependent term arises from the difference between the scattering lengths for $S = 0$ and 2 channels.[36] The inhomogeneous chemical potential μ_i is related to the uniform chemical potential μ and the quadratic, confining potential as in the spinless case (1). We set the scale of energies by choosing $zt = 1$.

B. Inhomogeneous mean-field theory

The mean-field theory that we use has been very successful in obtaining the phase diagrams for models (1) and (3), with $V_T = 0$, i.e., in the absence of the harmonic confining potential.[5,22] The inhomogeneous generalization of this theory, developed first for the Bose-glass phase[23] and spinless bosons, decouples the hopping term to obtain an effective one-site problem, neglects quadratic deviations from equilibrium values (denoted by angular brackets), uses the approximation

$$a^\dagger_i a_j \simeq \langle a^\dagger_i \rangle a_j + a^\dagger_i \langle a_j \rangle - \langle a^\dagger_i \rangle \langle a_j \rangle, \tag{4}$$

introduces the superfluid order parameter $\psi_i \equiv \langle a_i \rangle$ for the site i, and hence expresses the Hamiltonian (1) as $\mathcal{H}^{MF} = \sum_i \mathcal{H}^{MF}_i$, where the superscript MF denotes mean field and the single-site Hamiltonian is

$$\frac{\mathcal{H}^{MF}_i}{zt} = \frac{1}{2} \frac{U}{zt} \hat{n}_i(\hat{n}_i - 1) - \frac{\mu_i}{zt} \hat{n}_i - (\phi_i a^\dagger_i + \phi^*_i a_i) + \psi^*_i \phi_i. \tag{5}$$

Here, $\phi_i \equiv \frac{1}{z} \sum_\delta \psi_{i+\delta}$ and δ labels the z nearest neighbors of the site i. If $V_T = 0$, the effective onsite chemical potential $\mu_i = \mu$, for all i, so the local density and superfluid order parameters are independent of i: $\rho_i = \rho$ and $\psi_i = \psi$. If $V_T > 0$, we first obtain the matrix elements of $\mathcal{H}^{MF}_i$ in the onsite, occupation-number basis $\{|n_i\rangle\}$, truncated in practice by choosing a finite value for n_{max}, the total number of bosons per site, for a given initial set of values for $\{\psi_i\}$. (For small values of U, we must use large values of n_{max}; for the values of U we consider $n_{max} = 6$ suffices.) We then diagonalize this matrix, which depends on ψ_i and $\psi_{i+\delta}$, to obtain the lowest energy and the corresponding wave function denoted, respectively, by $E^i_g(\psi_i, \psi_{i+\delta})$ and $\Psi_g(\{\psi_i\})$; from these we obtain the new superfluid order parameters $\psi_i = \langle \Psi_g(\{\psi_i\})|a_i|\Psi_g(\{\psi_i\})\rangle$; we use these new values of ψ_i as inputs to reconstruct $\mathcal{H}^{MF}_i$ and repeat the diagonalization procedure until we achieve self-consistency of input and output values to obtain the equilibrium value ψ^{eq}_i (henceforth we suppress the superscript eq for notational convenience). [This is equivalent to a minimization of the total energy $E_g(\{\psi_i\}) \equiv \sum_i E^i_g(\psi_i, \psi_{i+\delta})$ with respect to ψ_i; if more than one solution is obtained, we pick the one that yields the global minimum.] The onsite density is obtained from $\rho_i = \langle \Psi_g(\{\psi_i\})|\hat{n}_i|\Psi_g(\{\psi_i\})\rangle$. In representative cases, we have found that the equilibrium value of ψ_i is real; so, henceforth, we restrict ourselves to real values of ψ_i.

For the two-species Hamiltonian (3), our mean-field theory obtains an effective, one-site problem by decoupling the two

hopping terms as follows [cf. Eq. (4)]:

$$a^\dagger_i a_j \simeq \langle a^\dagger_i \rangle a_j + a^\dagger_i \langle a_j \rangle - \langle a^\dagger_i \rangle \langle a_j \rangle,$$
$$b^\dagger_i b_j \simeq \langle b^\dagger_i \rangle b_j + b^\dagger_i \langle b_j \rangle - \langle b^\dagger_i \rangle \langle b_j \rangle. \tag{6}$$

Here, the superfluid order parameters for the site i for bosons of types a and b are $\psi_{ai} \equiv \langle a_i \rangle$ and $\psi_{bi} \equiv \langle b_i \rangle$, respectively. The approximation (6) can now be used to write the Hamiltonian (3) as a sum over single-site, mean-field Hamiltonians $\mathcal{H}^{MF}_i$ [cf. Eq. (5)] given below:

$$\frac{\mathcal{H}^{MF}_i}{zt} = \frac{1}{2} \frac{U_a}{zt} \hat{n}_{ai}(\hat{n}_{ai} - 1) - \frac{\mu_{ai}}{zt} \hat{n}_{ai} - (\phi_{ai} a^\dagger_i + \phi^*_{ai} a_i)$$
$$+ \psi^*_{ai} \phi_{ai} + \frac{1}{2} \frac{U_b}{zt} \hat{n}_{bi}(\hat{n}_{bi} - 1) - \frac{\mu_{bi}}{zt} \hat{n}_{bi}$$
$$- (\phi_{bi} b^\dagger_i + \phi^*_{bi} b_i) + \psi^*_{bi} \phi_{bi} + \frac{U_{ab}}{zt} \hat{n}_{ai} \hat{n}_{bi}. \tag{7}$$

Here, $\phi_{ai} \equiv \frac{1}{z} \sum_\delta \psi_{ai+\delta}$ and $\phi_{bi} \equiv \frac{1}{z} \sum_\delta \psi_{bi+\delta}$, where δ labels the nearest neighbors of the site i. If $V_T = 0$, the effective onsite chemical potentials $\mu_{ai} = \mu_a$ and $\mu_{bi} = \mu_b$, for all i, so $\rho_{ai} = \rho_a$, $\rho_{bi} = \rho_b$, $\psi_{ai} = \psi_a$, and $\psi_{bi} = \psi_b$ are independent of i.

If $V_T > 0$, we first obtain, for a given initial set of values for $\{\psi_{ai}\}$ and $\{\psi_{bi}\}$, the matrix elements of $\mathcal{H}^{MF}_i$ in the onsite, occupation-number basis $\{|n_{ai}\rangle, |n_{bi}\rangle\}$, which we truncate in a practical calculation by choosing a finite value n_{max} for the total number of bosons per site. (The smaller the values of the interaction parameters U_a, U_b, and U_{ab}, the larger must be the value of n_{max}; for the values of U_a, U_b, U_{ab}, μ_a, and μ_b that we consider, $n_{max} = 6$ suffices.) We then diagonalize this matrix, which depends on ψ_{ai}, ψ_{bi}, $\psi_{a(i+\delta)}$, and $\psi_{b(i+\delta)}$, to obtain the lowest energy and the corresponding wave function denoted, respectively, by $E^i_g(\psi_{ai}, \psi_{a(i+\delta)}; \psi_{bi}, \psi_{b(i+\delta)})$ and $\Psi_g(\{\psi_{ai}, \psi_{bi}\})$, whence we obtain the new superfluid order parameters $\psi_{ai} = \langle \Psi_g(\{\psi_{ai}, \psi_{bi}\})|a_i|\Psi_g(\{\psi_{ai}, \psi_{bi}\})\rangle$ and $\psi_{bi} = \langle \Psi_g(\{\psi_{ai}, \psi_{bi}\})|b_i|\Psi_g(\{\psi_{ai}, \psi_{bi}\})\rangle$; we use these new values of ψ_{ai} and ψ_{bi} as inputs to reconstruct $\mathcal{H}^{MF}_i$ and repeat the diagonalization procedure until we achieve self-consistency of input and output values to obtain the equilibrium value ψ^{eq}_{ai} and ψ^{eq}_{bi}; again, we suppress the superscript eq for notational convenience. [As we have mentioned in the single-species case, this self-consistency procedure is equivalent to a minimization, with respect to ψ_{ai} and ψ_{bi}, of the total energy $E_g(\{\psi_{ai}, \psi_{bi}\}) \equiv \sum_i E^i_g(\psi_{ai}, \psi_{ai+\delta}; \psi_{bi}, \psi_{bi+\delta})$; we pick the solution that yields the global minimum.] The onsite densities are obtained from $\rho_{ai} = \langle \Psi_g(\{\psi_{ai}, \psi_{bi}\})|\hat{n}_{ai}|\Psi_g(\{\psi_{ai}, \psi_{bi}\})\rangle$ and $\rho_{bi} = \langle \Psi_g(\{\psi_{ai}, \psi_{bi}\})|\hat{n}_{bi}|\Psi_g(\{\psi_{ai}, \psi_{bi}\})\rangle$, respectively. We follow our discussion of the mean-field theory of the BH model (1) and restrict ourselves to real values of ψ_{ai} and ψ_{bi}.

The inhomogeneous mean-field theory for the spin-1 BH model follows along similar lines. The spin-1 analogs of Eqs. (4) and (5) are, respectively,

$$a^\dagger_{i,\sigma} a_{j,\sigma} \simeq \langle a^\dagger_{i,\sigma} \rangle a_{j,\sigma} + a^\dagger_{i,\sigma} \langle a_{j,\sigma} \rangle - \langle a^\dagger_{i,\sigma} \rangle \langle a_{j,\sigma} \rangle \tag{8}$$

and

$$\frac{\mathcal{H}_i^{\text{MF}}}{zt} = \frac{1}{2}\frac{U_0}{zt}\hat{n}_i(\hat{n}_i - 1) + \frac{1}{2}\frac{U_2}{zt}\left(\vec{F}_i^2 - 2\hat{n}_i\right) - \frac{\mu_i}{zt}\hat{n}_i$$
$$- \sum_\sigma \left(\phi_{i,\sigma}a_{i,\sigma}^\dagger + \phi_{i,\sigma}^* a_{i,\sigma}\right) + \sum_\sigma \psi_{i,\sigma}^*\phi_{i,\sigma}. \quad (9)$$

Here, we use the following superfluid order parameters:

$$\psi_{i,\sigma} \equiv \langle a_{i,\sigma}\rangle, \quad (10)$$

and $\phi_{i,\sigma} \equiv \frac{1}{z}\sum_\delta \psi_{(i+\delta),\sigma}$, where and δ labels the z nearest neighbors of the site i; recall, furthermore, that σ can assume the values $1, 0, -1$, and $\hat{n}_{i,\sigma} \equiv a_{i,\sigma}^\dagger a_{i,\sigma}$, $\hat{n}_i \equiv \sum_\sigma \hat{n}_{i,\sigma}$, and $\vec{F}_i = \sum_{\sigma,\sigma'} a_{i,\sigma}^\dagger \vec{F}_{\sigma,\sigma'} a_{i,\sigma'}$ with $\vec{F}_{\sigma,\sigma'}$ standard spin-1 matrices. With these order parameters [cf. Eq. (10)] we have developed an inhomogeneous version of the homogeneous mean-field theory[22] for the spin-1 BH model with $V_T = 0$.

The self-consistency procedure that we use now is similar to, but more complicated than, the one we have used for the spinless BH model. If $V_T > 0$, we first obtain, for a given initial set of values for $\{\psi_{i,\sigma}\}$, the matrix elements of $\mathcal{H}_i^{\text{MF}}$ in the onsite, occupation-number basis $\{|n_{i,-1}, n_{i,0}, n_{i,1}\rangle\}$, truncated in a practical calculation by choosing a finite value for $n_{\max}$, the total number of bosons per site. (For small values of U and U_2, we must use large values of $n_{\max}$; for the values we use here, $n_{\max} = 4$ suffices.] We then diagonalize this matrix, which depends on $\psi_{i,\sigma}$ and $\psi_{(i+\delta),\sigma}$, to obtain the lowest energy and the corresponding wave function, denoted, respectively, by $E_g^i(\psi_{i,\sigma}, \psi_{(i+\delta),\sigma})$ and $\Psi_g(\{\psi_{i,\sigma}\})$; from these we obtain the new superfluid order parameters $\psi_{i,\sigma} = \langle \Psi_g(\{\psi_{i,\sigma}\})|a_{i,\sigma}|\Psi_g(\{\psi_{i,\sigma}\})\rangle$; we use these new values of $\psi_{i,\sigma}$ to reconstruct $\mathcal{H}_i^{\text{MF}}$ and repeat the diagonalization procedure until input and output values are self-consistent; thus, we obtain the equilibrium value $\psi_{i,\sigma}^{\text{eq}}$. We suppress eq as above and recall that this self-consistent procedure is equivalent to a minimization of the total energy in the spin-1 case.[22] Here, too, we follow our discussion of the mean-field theory of the BH model (1) and restrict ourselves to real values of $\psi_{i,\sigma}$.

We have noted in an earlier study[22] that, at the level of our mean-field theory, the superfluid density in the spin-1 case is

$$\rho_s = \sum_\sigma \left|\psi_\sigma^{\text{eq}}\right|^2, \quad (11)$$

and the magnetic properties of the SF phases follow from[20,21]

$$\langle \vec{F}\rangle = \frac{\sum_{\sigma,\sigma'} \psi_\sigma^{\text{eq}} \vec{F}_{\sigma,\sigma'} \psi_{\sigma'}^{\text{eq}}}{\sum_\sigma \left|\psi_\sigma^{\text{eq}}\right|^2}. \quad (12)$$

If we substitute the explicit forms of the spin-1 matrices, we obtain

$$\langle \vec{F}\rangle = \sqrt{2}\frac{(\psi_1\psi_0 + \psi_{-1}\psi_0)}{\sum_\sigma |\psi_\sigma|^2}\hat{x} + \frac{(\psi_1^2 - \psi_{-1}^2)}{\sum_\sigma |\psi_\sigma|^2}\hat{z},$$
$$\langle \vec{F}\rangle^2 = 2\frac{(\psi_1\psi_0 + \psi_{-1}\psi_0)^2}{\left(\sum_\sigma |\psi_\sigma|^2\right)^2} + \frac{(\psi_1^2 - \psi_{-1}^2)^2}{\left(\sum_\sigma |\psi_\sigma|^2\right)^2}, \quad (13)$$

where $\hat{x}$ and $\hat{z}$ are unit vectors in spin space; SF phases with $\langle \vec{F}\rangle = 0$ and $\langle \vec{F}\rangle^2 = 1$ are referred to as polar and

ferromagnetic, respectively. The order-parameter manifolds of these phases can be found in earlier studies.[21,22]

III. RESULTS

Given the formalism we have described above, we can obtain several results for quantities that have been measured in quantum Monte Carlo (QMC) simulations or in experiments for the spinless case. We cover this in Sec. III A. Section III B is devoted to the results of our inhomogeneous MF theory for the case with two types of bosons. In Sec. III C, we present the results of our inhomogeneous MF theory for the spin-1 case.

A. Results for the spinless Bose-Hubbard model

First, we compare our mean-field-theory (MFT) results with those obtained by quantum Monte Carlo simulations in two dimensions.[24] These simulations use $U/t = 25$, $\mu/U = 0.37$, and $V_T/U = 0.002$, and obtain the local density ρ_i and the local compressibility $\kappa_i^{\text{local}} = \partial\rho_i/\partial\mu_i$. For this set of parameters, we calculate ρ_i and thence κ_i^{local}; we also obtain the local superfluid density $\rho_i^s \equiv \psi_i^2$ (the last formula is valid at the level of our MF theory). In Fig. 1, we plot versus R_i our MF results for ρ_i, κ_i^{local}, and ρ_i^s along with data from QMC simulations.[24] For this set of parameters, the central region near the origin of the lattice is in the MI phase, i.e., the local density $\rho_i = 1$ and both ρ_i^s and κ_i^{local} vanish. This central core is enveloped by an SF shell, with nonzero values for ρ_i^s and κ_i^{local}. As we move radially outward from the center, ρ_i decreases monotonically until it goes to zero, as do ρ_i^s and κ_i^{local}, in the region where $\mu_i^{\text{eff}} < 0$. The quantitative agreement between our MFT results and those from QMC is shown in Fig. 1; there is only a slight discrepancy between the MFT
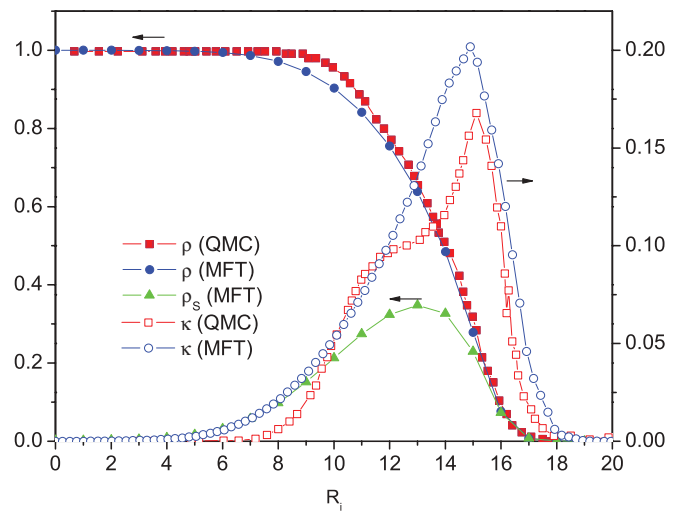

FIG. 1. (Color online) Plots of our mean-field-theory (MFT) results for the local density n_i versus R_i (blue filled circles), local compressibility $\kappa_i^{\text{local}} = \partial n/\partial\mu^{\text{eff}}$ (blue open circles), and local superfluid density $\rho_i^s = \psi_i^2$ (green filled triangles) of spinless bosons in a two-dimensional parabolic trap with $V_T/U = 0.002$, $\mu/U = 0.37$, and $U/t = 25$. We also compare our results with those of QMC for which we have obtained data by digitizing plots in figures in simulation studies (Ref. 24) for n_i (red filled squares) and κ_i^{local} (red open squares).
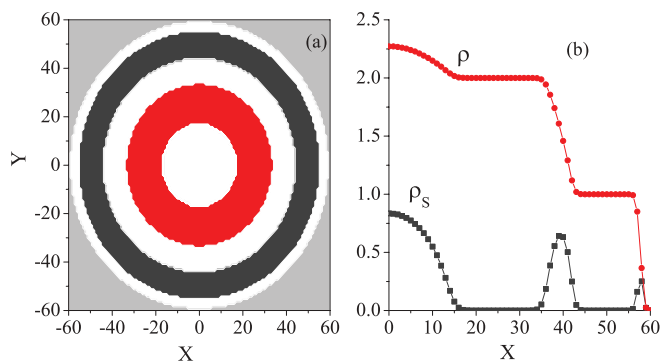
FIG. 2. (Color online) (a) SF (white) and MI regions [$\rho = 2$ (red) and $\rho = 1$ (black)] annuli formed in a 2D planar section $\mathcal{P}_Z$ through the 3D lattice, at a vertical distance Z from the center (here $Z = 0$) and (b) the corresponding radial variation of density ρ_i (red circles) and superfluid density ρ_i^s (black squares) for $\mu/E_r = 1$, $V_T/E_r = 0.0003$, and $V_0 = 15E_r$; the outermost gray regions in (a) contain no bosons.

ρ_i and its QMC analog at the MI-SF interface; our result for κ_i^{local} also seems to miss, at this interface, the shoulder that appears in the QMC κ_i^{local} perhaps because our MFT theory overestimates the stability of the SF phase.

This good agreement between our MFT results and those of QMC simulations has encouraged us to use our MFT in cases where such simulations pose a significant numerical challenge. In particular, we use our theory to make direct comparisons with experiments[26] that have observed alternating MI and SF shells in 3D optical lattices by recording in-trap density distributions of bosons at different filling fractions. We use a simple-cubic lattice with 121^3 sites, $\mu/E_r = 1$, $V_T/E_r = 0.0003$, and the optical potential V_0/E_r in the range 12–16 so that the number of bosons $N \simeq 10^6$, which is comparable to the number of atoms in the experiments[26] we consider. This choice of parameters leads to two well-developed MI shells ($\rho = 1$ and 2, respectively). The MI and SF shells appear as annuli[26] in a two-dimensional (2D) planar section $\mathcal{P}_Z$ through the 3D lattice, at a vertical distance Z from the center [see, e.g., Fig. 2(a) for $V_0/E_r = 15$ and $Z = 0$ where the core region is in the SF phase]. Figure 2(b) shows that, as we move radially outward, ρ_i decreases monotonically and ρ_i^s is zero in the two MI regimes ($16 < R_i < 34$ and $44 < R_i < 52$) in which ρ_i is pinned at 2 and 1, respectively. SF and MI shells alternate and the outermost one is always in the SF phase; their positions and radii depend on μ, which also controls the total number N of atoms in the system, as illustrated by the $\mathcal{P}_{Z=0}$ sections in Figs. 3(a) and 3(b) for $V_0/E_r = 15$ and $\mu = 0.8$ ($N = 7.1 \times 10^5$) and $\mu = 0.9$ ($N = 8.9 \times 10^5$), respectively. For any 2D planar section $\mathcal{P}_Z$, we can calculate $N_m(Z)$, the number of bosons in the $\rho = m$ MI annulus, and $N_m^r(Z)$, the remaining number of bosons; the total number of bosons in this planar section is $N(Z) = N_m(Z) + N_m^r(Z)$, which does not depend on m. In Figs. 3(c) and 3(d) we show, for $m = 2$ and $\mu = 0.8$ and 0.9, respectively, plots versus Z of $N_m(Z)$ (full red squares), $N_m^r(Z)$ (full blue triangles), and their sum $N(Z)$ (full black circles). Figures 2(c) and 2(d) are remarkably similar to the density profiles obtained in experiments[26] [cf. their Figs. 3(c) and 3(d)].
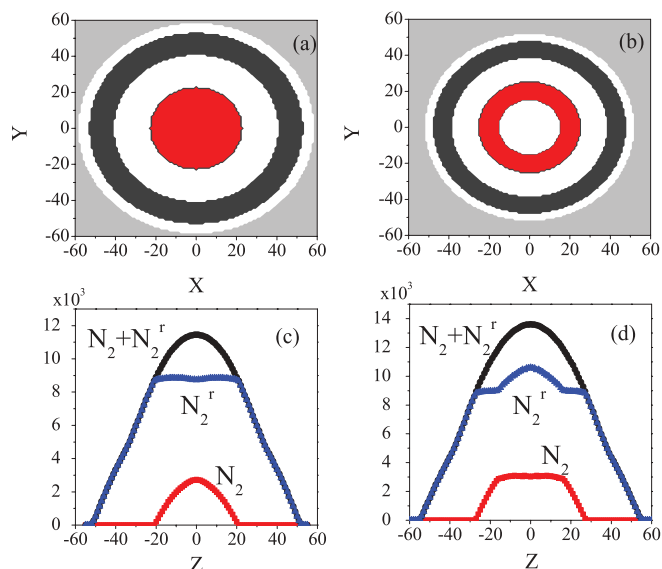

FIG. 3. (Color online) SF (white) and MI regions [$\rho = 2$ (red) and $\rho = 1$ (black)] annuli formed in the 2D $\mathcal{P}_{Z=0}$ sections in (a) and (b) for $V_0/E_r = 15$, $V_T/E_r = 0.0003$, and (a) $\mu/E_r = 0.8$ ($N = 7.1 \times 10^5$) and (b) $\mu/E_r = 0.9$ ($N = 8.9 \times 10^5$). The corresponding integrated in-trap density profiles $N_2(Z)$ (red squares), $N_2^r(Z)$ (blue squares), and $N_2 + N_2^r$ (black circles) are shown, respectively, in (c) and (d); these figures are qualitatively similar to Figs. 3(c) and 3(d) in a recent experimental study (Ref. 26).

The radii of MI shells follow from such in-trap density profiles: In Figs. 4(a) and 4(b), we plot $N_m(Z)$ and $N_m^r(Z)$ versus Z for $m = 2$ and 1, respectively, with
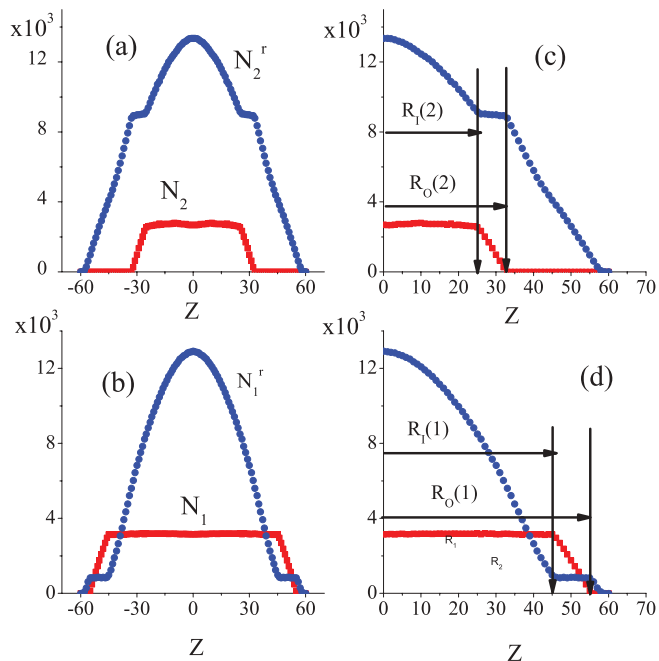

FIG. 4. (Color online) (a) and (b) Plots of $N_m(Z)$ (red squares) and N_m^r (blue circles) versus Z for $m = 2$ and 1, respectively, with $\mu/E_r = 1$; the plots in (c) and (d), which are the same as the right halves of (a) and (b), respectively, show how we determine the inner and outer radii [$R_I(m)$ and $R_O(m)$, respectively] from the plateaux in $N_m(Z)$ and $N_m^r(Z)$.

$\mu/E_r = 1$. The curves $N_m(Z)$ show nearly flat plateaux for $-R_I(m) \leqslant Z \leqslant R_I(m)$; similar plateaux occur in $N_m^r(Z)$ for $R_I(m) \leqslant |z| \leqslant R_O(m)$ [Figs. 4(a), 4(c), and 4(b), 4(d) for $m = 2$ and 1, respectively]. Here, $R_I(m)$ and $R_O(m)$ are the inner and outer radii of the MI shell with integer density m. Elementary geometry can be used to surmise the existence of these plateaux from the MI-SF shell structure[22] as we show below.

$N_m(Z)$ is m times the total number of sites inside the $\rho = m$ MI annulus; this number of sites is well approximated by the area $A(Z,m)$ of this annulus. Thus,

$$N_m(Z) = m A(Z,m) = m\pi \left[R_O^2(Z,m) - R_I^2(Z,m) \right], \quad (14)$$

where $R_O(Z,m)$ and $R_I(Z,m)$ are, respectively, the outer and inner radii of the MI annulus with density $\rho = m$, in the 2D planar section $\mathcal{P}_Z$. If $Z < R_I(m)$, simple geometry yields $R_I^2(Z,m) = R_I^2(m) - Z^2$ and $R_O^2(Z,m) = R_O^2(m) - Z^2$; therefore,

$$N_m(Z) = m\pi \left[R_O^2(m) - R_I^2(m) \right], \quad (15)$$

whence we conclude that $N_m(Z)$ is independent of Z when $|Z| < R_I(m)$; this result yields the plateaux in the in-trap density profiles shown in Figs. 4(a)–4(d); if $|Z| > R_O(m)$, the 2D planar section has no MI shell with density m, thus, $N_m(Z) = 0$, which is also apparent in these figures. For $Z < R_I(m)$, the central parts of the 2D planar sections $\mathcal{P}_Z$ show SF

shells and $N_m^r = N(Z) - N_m(Z)$ decreases as we increase Z. For $R_I(m) < Z < R_O(m)$, the central parts of the 2D planar sections $\mathcal{P}_Z$ show MI shells; the number of bosons in such MI shells is $N_m(Z)$ and it is proportional to the area of this central shell, namely, $m\pi [R_O^2(m) - Z^2]$; thus, $N_m(Z)$ decreases as we increase Z here; however, $N_m^r = N(Z) - N_m(Z)$ remains independent of Z because of the simple geometrical arguments given above; i.e., we have plateaux in $N_m^r(Z)$ in the region $R_I(m) < Z < R_O(m)$. Finally, for $Z > R_O(m)$, the 2D planar section $\mathcal{P}_Z$ has no MI shell with density m, from which it follows that $N_m(Z) = 0$.

In Fig. 5(a), we plot, for $m = 1$ and 2, $R_O(m)$ and $R_I(m)$, which we have determined from plots such as those in Figs. 4(c) and 4(d), versus $V_0(E_r)$; the MI phase with $\rho = m$ lies between the curves $R_O(m)$ and $R_I(m)$. Figure 5(a) can be used to obtain the phase diagram of the homogeneous Bose-Hubbard model as follows: $\mu_i = \mu - V_T R_i^2$, so $R_O(m)$ and $R_I(m)$ can be used to obtain $\mu^-(m) = \mu - V_T R_O^2(m)$ and $\mu^+(m) = \mu - V_T R_I^2(m)$, which are, respectively, the lower and upper boundaries of the Mott lobe with density $\rho = m$. The resulting Mott lobe [obtained by the conversion $V_0(E_r) \rightarrow U/zt$] is given in Fig. 5(b) along with its counterpart for the *homogeneous* Bose-Hubbard model, which we have obtained from the homogeneous mean-field theory;[5] the agreement between these lobes is striking and it encourages us to suggest that the phase diagram of the homogeneous Bose-Hubbard model can be obtained from the inner and outer radii of the MI shells. Thus, experiments on cold atoms in optical lattices *with a quadratic confining potential*[26] can be used directly to obtain the phase diagram of the *homogeneous* Bose-Hubbard model from $R_O(m)$ and $R_I(m)$, which can be determined for
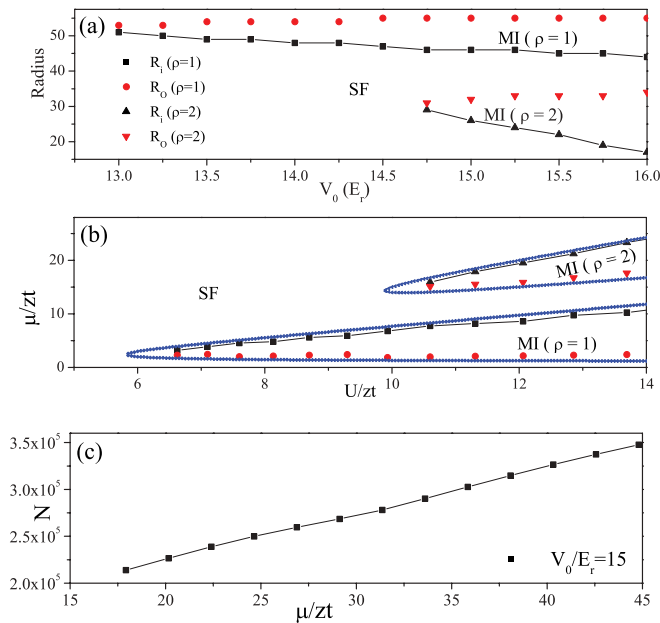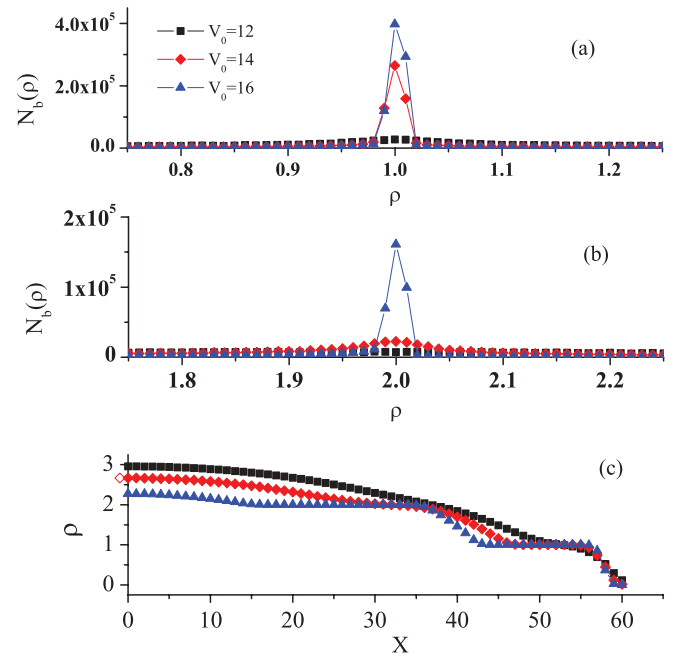

FIG. 5. (Color online) (a) Plots, for $\rho = m = 1$ and 2, of $R_O(m)$ and $R_I(m)$ versus $V_0(E_r)$; the MI phase with $\rho = m$ lies between the curves $R_O(m)$ and $R_I(m)$; red circles and red inverted triangles denote $R_O(1)$ and $R_O(2)$, respectively; and black squares and black triangles denote $R_I(1)$ and $R_I(2)$, respectively; (b) Mott insulating lobes, in plots of $\mu^+(m) = \mu - V_T R_I^2(m)$ and $\mu^-(m) = \mu - V_T R_O^2(m)$ for $m = 2$ and 1 versus $U/(zt)$ [obtained by the conversion $V_0(E_r) \rightarrow U/(zt)$]; we use the same symbols as in (a); we show, for comparison, the boundaries of the MI lobes for $m = 1$ (blue diamonds) and $m = 2$ (blue triangles) that follow from our mean-field theory for the *homogeneous* Bose-Hubbard model (Ref. 5). (c) An illustrative plot of the total number of bosons N in the system versus the chemical potential μ.

FIG. 6. (Color online) Representative plots of $N_b(\rho)$, the number of bosons in the system with a given density ρ, versus ρ near (a) $\rho = 1$ and (b) $\rho = 2$ for $V_0 = 12E_r$ (black squares), $14E_r$ (red diamonds), and $16E_r$ (blue triangles). (c) The radial variation of density ρ_i for $V_0 = 12E_r$ (black squares), $14E_r$ (red diamonds), and $16E_r$ (blue triangles).

an MI shell with density $\rho = m$ as described above. Note that (a) $\mu^-(m)$ and $\mu^+(m)$ are fixed for a given $V_0(E_r)$ and (b) the total number of bosons N increases linearly with the chemical potential μ [see Fig. 5(c)]. Therefore, the inner and outer radii of the MI shell $R_{O,I}(m) = \sqrt{(\mu - \mu^{-,+}/V_T)}$ are proportional to $\sqrt{N}$, for fixed V_T and V_0; this proportionality has been reported in recent experiments[26] (cf. their Fig. 3).

Images of MI shells have been obtained recently from atomic-clock-shift experiments.[27] By using the density-dependent transition-frequency shifts, sites with different densities of bosons can be distinguished spectroscopically and, therefore, MI shells, with different values of the integer density m, are revealed as peaks in the occupation number at the corresponding frequencies. This experiment gives $N_b(\rho)$, the number of bosons in the system at a given density ρ. We use our inhomogeneous mean-field theory to obtain $N_b(\rho)$, and in Figs. 6(a) and 6(b) we plot $N_b(\rho)$ (with ρ close to $m = 1$ and 2, respectively) for $V_0/E_r = 12$, 14, and 16, with $V_T/E_r = 0.0003$ and $\mu/E_r = 1$. The SF and MI shell structure is evident from the radial variation of the local density given in Fig. 6(c). For $V_0 = 12E_r$, no Mott shell is present; this is reflected in a flat variation of $N_b(\rho)$ for all ρ. However, if $V_0 = 14E_r$, there is a well-formed MI shell $\rho = 1$; this can be inferred from the peak in $N_b(\rho)$ at $\rho = 1$. As V_0 increases, more Mott shells, with higher integral values of ρ, appear. This

behavior of $N_b(\rho)$ is in accordance with recent experiments[27] (cf. their Fig. 1).

B. Results for the Bose-Hubbard model with two species of bosons

We begin with an investigation of representative phase diagrams of the Bose-Hubbard model (3), with two species of bosons, in the homogeneous case, i.e., with $V_{Ta} = V_{Tb} = V_T = 0$. These have been explored to some extent in earlier theoretical studies[9–13] and Monte Carlo simulations,[16,17] but not over as wide a range of parameters as we consider here. Next, we use the inhomogeneous mean-field theory that we have developed above to explore order-parameter profiles and a variety of MI and SF shells that are obtained when we have a quadratic trap potential. We also present Fourier transforms of one-dimensional sections of these profiles.

First, we consider the case $U_{ab} < U_a = U_b$ and $\mu_a = \mu_b = \mu$ in which the order parameters and densities for both types of bosons show the same dependence on μ. In the first row of Fig. 7, we show the phase diagram [Fig. 7(a)] and plots versus μ of the order parameters ψ_a (red line) and ψ_b (blue dashed line) and the densities ρ_a (green dashed line) and ρ_b (pink full line) for $U_{ab} = 0.5U_a$, $U_a = U_b$, and $\mu_a = \mu_b = \mu$ and $U_a = 9$ [Fig. 7(b)], $U_a = 11$ [Fig. 7(c)],
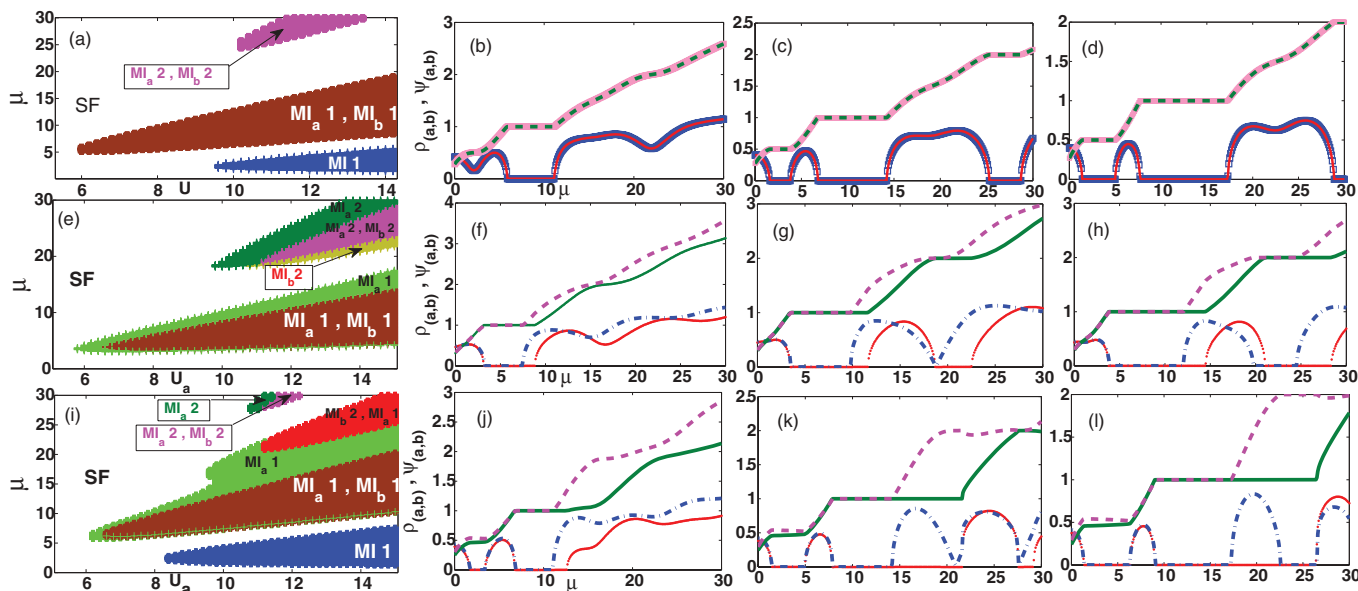

FIG. 7. (Color online) Phase diagram (a) and plots versus μ of the order parameters ψ_a (red line) and ψ_b (blue dashed line) and the densities ρ_a (green dashed line) and ρ_b (pink full line) for $U_{ab} = 0.5U_a$, $U_a = U_b$, and $\mu_a = \mu_b = \mu$ and $U_a = 9$ (b), $U_a = 11$ (c), and $U_a = 13$ (d). (We do not divide explicitly by zt because we set $zt = 1$.) The phase diagram shows an SF phase in which both species are superfluid; the blue MI1 lobe denotes a Mott insulating phase in which the density $\rho = 1$ is attained by having $\rho_a = \rho_b = 1/2$; the brown MI$_a$1,MI$_b$1 lobe denotes a Mott insulating phase in which the densities $\rho_a = \rho_b = 1$; the pink MI$_a$2,MI$_b$2 lobe denotes a Mott insulating phase in which the densities $\rho_a = \rho_b = 2$. In the second row, we show the phase diagram (e) and plots versus μ of the order parameters ψ_a and ψ_b and the densities ρ_a and ρ_b for $U_{ab} = 0.2U_a$, $U_b = 0.9U_a$, and $\mu_a = \mu_b = \mu$ and $U_a = 9$ (f), $U_a = 11$ (g), and $U_a = 13$ (h). The phase diagram shows an SF phase and brown MI$_a$1,MI$_b$1 and pink MI$_a$2,MI$_b$2 lobes; these are like their counterparts in (a). In addition, we have the following phases: (i) a green sliver MI$_a$1 in which bosons of type a are in an MI phase with $\rho_a = 1$ and bosons of type b are superfluid; (ii) a green ochre region MI$_b$2 in which bosons of type b are in an MI phase with $\rho_b = 2$ and bosons of type a are superfluid; and (iii) a dark green region MI$_a$2 in which bosons of type a are in an MI phase with $\rho_a = 2$ and bosons of type b are superfluid. In the third row, we show the phase diagram (i) and plots versus μ of the order parameters ψ_a and ψ_b and the densities ρ_a and ρ_b for $U_{ab} = 0.6U_a$, $U_b = 0.9U_a$, and $\mu_a = \mu_b = \mu$ and $U_a = 9$ (j), $U_a = 11$ (k), and $U_a = 13$ (l). The phase diagram shows the following: an SF phase; blue MI1, brown MI$_a$1,MI$_b$1, and pink MI$_a$2,MI$_b$2 lobes; green MI$_a$1 and dark green MI$_a$2 regions are like their counterparts in (a) and (e). In addition, we have a red MI$_b$2,MI$_a$1 lobe in which $\rho_b = 2$ and $\rho_a = 1$.

and $U_a = 13$ [Fig. 7(d)]. (We do not divide explicitly by zt, because we set $zt = 1$.) The phase diagram shows an SF phase in which both species are superfluid; the blue MI1 lobe denotes a Mott insulating phase in which the density $\rho = 1$ is attained by having $\rho_a = \rho_b = 1/2$; the brown MI$_a$1,MI$_b$1 lobe denotes a Mott insulating phase in which $\rho_a = \rho_b = 1$; the pink MI$_a$2,MI$_b$2 lobe denotes a Mott insulating phase with $\rho_a = \rho_b = 2$. Such phase diagrams can be obtained from plots like those in Figs. 7(b)–7(d).

In the second row of Fig. 7, we show the phase diagram [Fig. 7(e)] and plots versus μ of the order parameters ψ_a and ψ_b and the densities ρ_a and ρ_b for $U_{ab} = 0.2U_a$, $U_b = 0.9U_a$, and $\mu_a = \mu_b = \mu$ and $U_a = 9$ [Fig. 7(f)], $U_a = 11$ [Fig. 7(g)], and $U_a = 13$ [Fig. 7(h)]. The phase diagram shows an SF phase and brown MI$_a$1,MI$_b$1 and pink MI$_a$2,MI$_b$2 lobes; these are like their counterparts in Fig. 7(a). In addition, we have the following phases: (i) a green sliver MI$_a$1 in which bosons of type a are in an MI phase with $\rho_a = 1$ and bosons of type b are superfluid; (ii) a green ochre region MI$_b$2 in which bosons of type b are in an MI phase with $\rho_b = 2$ and bosons of type a are superfluid; and (iii) a dark green region MI$_a$2 in which bosons of type a are in an MI phase with $\rho_a = 2$ and bosons of type b are superfluid.

In the third row of Fig. 7, we show the phase diagram [Fig. 7(i)], and plots versus μ of the order parameters ψ_a and ψ_b and the densities ρ_a and ρ_b for $U_{ab} = 0.6U_a$,

$U_b = 0.9U_a$, and $\mu_a = \mu_b = \mu$ and $U_a = 9$ [Fig. 7(j)], $U_a = 11$ [Fig. 7(k)], and $U_a = 13$ [Fig. 7(l)]. The phase diagram shows the following: an SF phase; blue MI1, brown MI$_a$1,MI$_b$1, and pink MI$_a$2,MI$_b$2 lobes; green MI$_a$1 and dark green MI$_a$2 regions; these are like their counterparts in Figs. 7(a) and 7(e). In addition, we have a red MI$_b$2,MI$_a$1 lobe in which $\rho_b = 2$ and $\rho_a = 1$.

Next, we consider the case $U_{ab} < U_a$, $U_b = U_a$, and $\mu_b = 0.75\mu_a$. Specifically, in the first row of Fig. 8, we show the phase diagram [Fig. 8(a)], and plots versus μ_a of the order parameters ψ_a (red line) and ψ_b (blue dashed line) and the densities ρ_a (green full line) and ρ_b (pink dashed line) for $U_{ab} = 0.1U_a$, $U_a = U_b$, and $\mu_b = 0.75\mu_a$ and $U_a = 9$ [Fig. 8(b)], $U_a = 11$ [Fig. 8(c)], and $U_a = 13$ [Fig. 8(d)]. (We do not divide explicitly by zt because we set $zt = 1$.) The phase diagram shows an SF phase and brown MI$_a$1,MI$_b$1, pink MI$_a$2,MI$_b$2, and red MI$_a$2,MI$_b$1 lobes; green MI$_a$1, dark green MI$_a$2, and green ochre MI$_b$2 regions are like their counterparts in Figs. 7(a) and 7(e). In addition, we have a light blue region MI$_b$1 in which bosons of type b are in an MI phase with $\rho_b = 1$ and bosons of type a are superfluid.

In the second row of Fig. 8, we show the phase diagram [Fig. 8(e)] and plots versus μ_a of the order parameters ψ_a and ψ_b and the densities ρ_a and ρ_b for $U_{ab} = 0.3U_a$, $U_b = U_a$, and $\mu_b = 0.75\mu_a$ and $U_a = 9$ [Fig. 8(f)], $U_a = 11$ [Fig. 8(g)], and $U_a = 13$ [Fig. 8(h)]. This phase diagram shows the following:
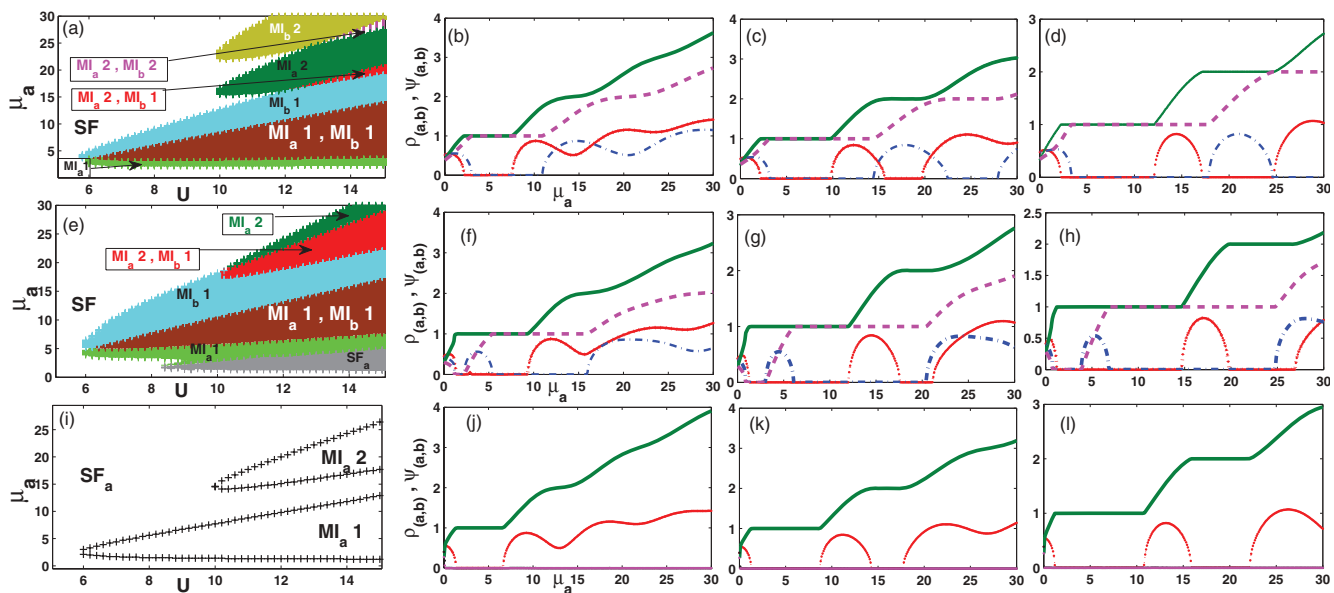

FIG. 8. (Color online) Phase diagram (a) and plots versus μ_a of the order parameters ψ_a (red line) and ψ_b (blue dashed line) and the densities ρ_a (green full line) and ρ_b (pink dashed line) for $U_{ab} = 0.1U_a$, $U_a = U_b$, and $\mu_b = 0.75\mu_a$ and $U_a = 9$ (b), $U_a = 11$ (c), and $U_a = 13$ (d). (We do not divide explicitly by zt because we set $zt = 1$.) The phase diagram shows an SF phase and brown MI$_a$1,MI$_b$1, pink MI$_a$2,MI$_b$2, and red MI$_a$2,MI$_b$1 lobes; green MI$_a$1, dark green MI$_a$2, and a green ochre MI$_b$2 regions are like their counterparts in Figs. 7(a) and 7(e). In addition, we have a light blue region MI$_b$1 in which bosons of type b are in an MI phase with $\rho_b = 1$ and bosons of type a are superfluid. In the second row, we show the phase diagram (e) and plots versus μ_a of the order parameters ψ_a and ψ_b and the densities ρ_a and ρ_b for $U_{ab} = 0.3U_a$, $U_b = U_a$, and $\mu_b = 0.75\mu_a$ and $U_a = 9$ (f), $U_a = 11$ (g), and $U_a = 13$ (h). The phase diagram shows the following: an SF phase; brown MI$_a$1,MI$_b$1 and red MI$_a$2,MI$_b$1 lobes; green MI$_a$1, dark green MI$_a$2, and light-blue MI$_b$1 regions are like their counterparts in (a). In addition, we have an SF$_a$ phase in which bosons of type a are in an SF phase and the boson density of type b has vanished. In the third row, we show the phase diagram (i) and plots versus μ_a of the order parameters ψ_a and ψ_b and the densities ρ_a and ρ_b for $U_{ab} = 0.7U_a$, $U_b = U_a$, and $\mu_b = 0.75\mu_a$ and $U_a = 9$ (j), $U_a = 11$ (k), and $U_a = 13$ (l). The phase diagram shows the following: an SF$_a$ phase; MI$_a$1 and MI$_a$2 regions are like their counterparts in (a) and (e) in which the boson density of type b has vanished.
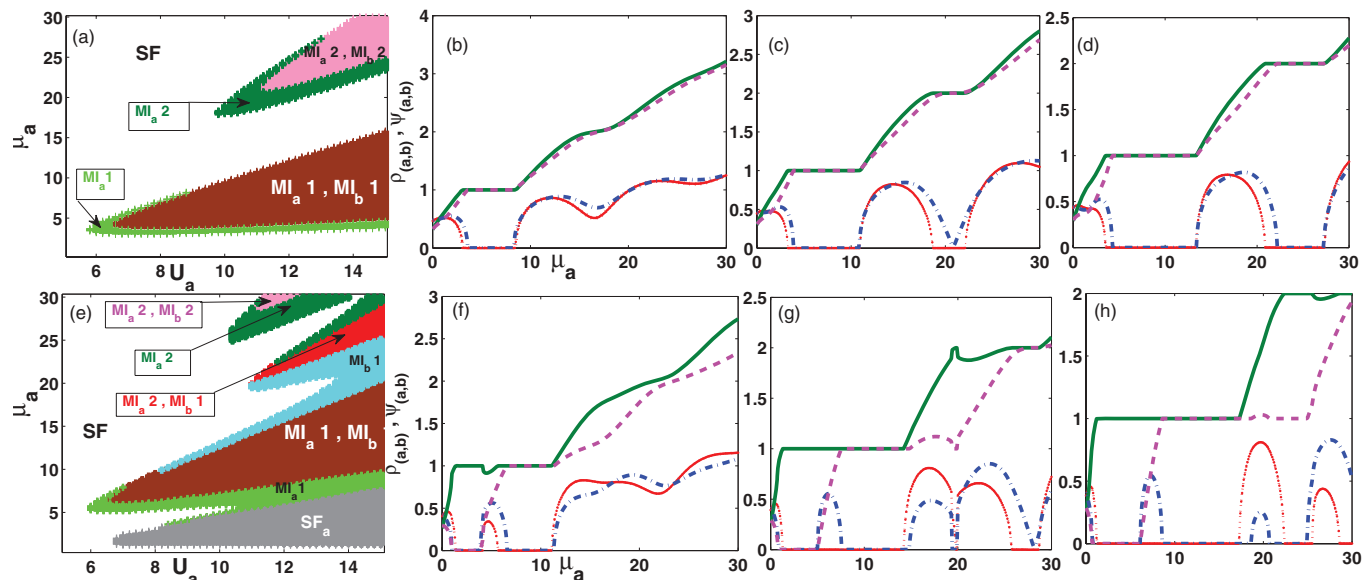
FIG. 9. (Color online) The phase diagrams (a) and (e) show the following: an SF phase and SF_a; brown MI_a1,MI_b1, red MI_a2,MI_b1, and pink MI_a2,MI_b2 lobes; green MI_a1, dark green MI_a2, and light blue MI_b1 regions; these are like their counterparts in Figs. 8(a) and 8(e). Plots versus μ_a of the order parameters ψ_a (red dashed line) and ψ_b (blue full line) and the densities ρ_a (green dashed line) and ρ_b (pink line) for $U_{ab} = 0.5U_a$, $U_b = 0.9U_a$, and $\mu_b = 0.9\mu_a$ and $U_a = 9$ (b) and (f), $U_a = 11$ (c) and (g), and $U_a = 13$ (d) and (h).

an SF phase; brown MI_a1,MI_b1 and red MI_a2,MI_b1 lobes; and green MI_a1, dark green MI_a2, and light blue MI_b1 regions are like their counterparts in Fig. 8(a). In addition, we have a dark gray SF_a phase in which bosons of type a are in an SF phase and the bosons of type b have vanished.

In the third row of Fig. 8, we show the phase diagram [Fig. 8(i)] and plots versus μ_a of the order parameters ψ_a and ψ_b and the densities ρ_a and ρ_b for $U_{ab} = 0.7U_a$, $U_b = U_a$, and $\mu_b = 0.75\mu_a$ and $U_a = 9$ [Fig. 8(j)], $U_a = 11$ [Fig. 8(k)], and $U_a = 13$ [Fig. 8(l)]. The phase diagram shows the following: an SF_a phase; and MI_a1 and MI_a2 regions that are like their counterparts in Figs. 8(a) and 8(e) in which the bosons density for type b has vanished.

We now consider the case $U_{ab} < U_a$, $U_b = 0.9U_a$, and $\mu_b = 0.9\mu_a$. Specifically, in the first row of Fig. 9, we show the phase diagram [Fig. 9(a)] and plots versus μ_a of the order parameters ψ_a (red line) and ψ_b (blue dashed line) and the densities ρ_a (green full line) and ρ_b (pink dashed line) for $U_{ab} = 0.2U_a$, $U_a = 0.9U_b$, and $\mu_b = 0.9\mu_a$ and $U_a = 9$ [Fig. 9(b)], $U_a = 11$ [Fig. 9(c)], and $U_a = 13$ [Fig. 9(d)]. The phase diagram shows an SF phase and brown MI_a1,MI_b1 and pink MI_a2,MI_b2 lobes; green MI_a1 and dark green MI_a2 are like their counterparts in Figs. 7, 8(a), and 8(e).

In the second row of Fig. 9, we show the phase diagram [Fig. 9(e)] and plots versus μ_a of the order parameters ψ_a and ψ_b and the densities ρ_a and ρ_b for $U_{ab} = 0.5U_a$, $U_b = 0.9U_a$, and $\mu_b = 0.9\mu_a$ and $U_a = 9$ [Fig. 9(f)], $U_a = 11$ [Fig. 9(g)], and $U_a = 13$ [Fig. 9(h)]. The phase diagram shows the following: an SF phase and SF_a; brown MI_a1,MI_b1, red MI_a2,MI_b1, and pink MI_a2,MI_b2 lobes; green MI_a1, dark green MI_a2, and light blue MI_b1 regions are like their counterparts in Figs. 8(a) and 8(e).

We now consider the effect of a parabolic potential and use the inhomogeneous mean-field theory, developed in the previ-

ous section, to obtain alternating spherical shells of the variety of MI and SF phases, shown in the phase diagrams in Figs. 7–9, for the two-species BH model (3). We do this by obtaining the order-parameter profiles $\{\psi_{ai},\rho_{ai}; \psi_{bi},\rho_{bi}\}$ and also by obtaining in-trap density distributions of bosons at representative values of U_{ab}, U_a, U_b, and $\mu_a = \mu_b$. In particular, we use a 3D simple-cubic lattice with 128^3 sites and $V_T/(zt) = 0.008$, and we study the following representative case: $\mu_a/(zt) = \mu_b/(zt) = 30$, $U_{ab} = 0.6U_a$, $U_b = 0.9U_a$, when $U_a/(zt) = 13$. With these parameters, the total number of bosons $N_T \simeq 10^6$, which is comparable to experimental values. Furthermore, this choice of parameters leads not only to SF shells but also to two well-developed MI shells (MI1 and MI2).

We show representative plots of the densities ρ_a (green dashed line) and ρ_b (pink line) versus the position X along the line $Y = Z = 0$ in Fig. 10 for $\mu_a = \mu_b = 30$, $V_T/(zt) = 0.008$, and the following six parameter sets, respectively: (a) $U_a/(zt) = 8$, $U_b = 0.9U_a$, and $U_{ab} = 0.6U_a$, (b) $U_a/(zt) = 10$, $U_b = 0.9U_a$, and $U_{ab} = 0.6U_a$, (c) $U_a/(zt) = 11$, $U_b = 0.9U_a$, and $U_{ab} = 0.6U_a$, (d) $U_a/(zt) = 12$, $U_b = 0.9U_a$, and $U_{ab} = 0.6U_a$, (e) $U_a/(zt) = 13$, $U_b = 0.9U_a$, and $U_{ab} = 0.6U_a$, and (f) $U_a/(zt) = 14$, $U_b = 0.9U_a$, and $U_{ab} = 0.6U_a$. It is also useful to obtain a complementary, Fourier-representation picture of the profiles in Figs. 10(a)–10(f) because it might be possible to obtain them in time-of-flight measurements.[1] Three-dimensional transforms of the shell structure can be obtained, but they are not easy to visualize; therefore, we present the one-dimensional Fourier transforms of $\rho_a(X, Y = 0, Z = 0)$ and $\rho_b(X, Y = 0, Z = 0)$ with respect to X. The moduli of these transforms, namely, $|\rho_{a,k_X}|$ (green lines), and $|\rho_{b,k_X}|$ (pink lines) of the profiles in Figs. 10(a)–10(f) are plotted, respectively, in Figs. 11(a)–11(f) versus the wave vector k_X/π. The principal peaks in these transforms occur at $k_X = 0$ (or 2π); these are associated with
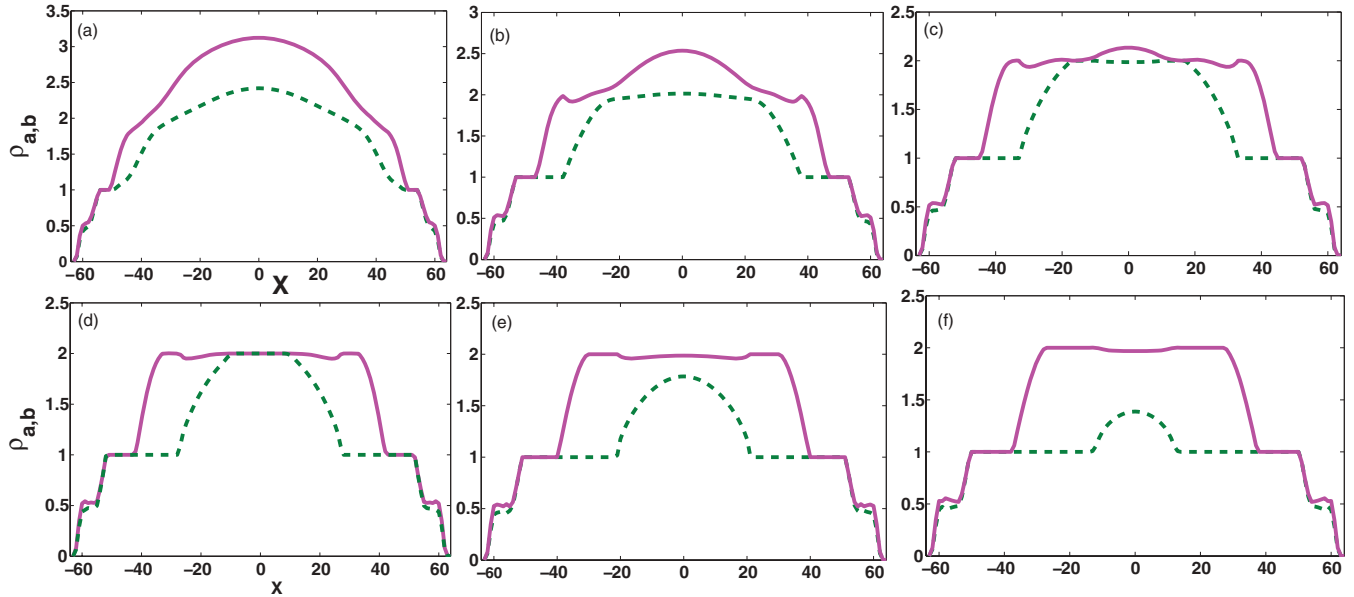
FIG. 10. (Color online) Plots of ρ_{ai} (green dashed line) and ρ_{bi} (pink line) versus X, along the $Y = Z = 0$ line, with $\mu_a = \mu_b = 30$, $V_T/(zt) = 0.008$, and (a) $U_a/(zt) = 8$, $U_b = 0.9U_a$, and $U_{ab} = 0.6U_a$, (b) $U_a/(zt) = 10$, $U_b = 0.9U_a$, and $U_{ab} = 0.6U_a$, (c) $U_a/(zt) = 11$, $U_b = 0.9U_a$, and $U_{ab} = 0.6U_a$, (d) $U_a/(zt) = 12$, $U_b = 0.9U_a$, and $U_{ab} = 0.6U_a$, (e) $U_a/(zt) = 13$, $U_b = 0.9U_a$, and $U_{ab} = 0.6U_a$, and (f) $U_a/(zt) = 14$, $U_b = 0.9U_a$, and $U_{ab} = 0.6U_a$.

the spatially uniform MI and SF phases. In an infinite system with no confining potential, these are the only peaks; however, the quadratic confining potential leads to shells of MI and SF phases (see below); this shell structure leads to the subsidiary peaks that appear in Figs. 11(a)–11(f) away from $k_X = 0$, and 2π.

We can also obtain order-parameter profile plots; these are shown in Figs. 12(a)–12(f) for the same parameter values as in Figs. 10(a)–10(f), respectively; in these plots, ψ_a is indicated

by a red dashed line and ψ_b by a blue line. We can also obtain the one-dimensional Fourier transforms of $\psi_a(X, Y = 0, Z = 0)$ and $\psi_b(X, Y = 0, Z = 0)$ with respect to X. The moduli of these transforms, namely, $|\psi_{a,k_X}|$ (red lines) and $|\psi_{b,k_X}|$ (blue lines) of the profiles Figs. 12(a)–12(f) are plotted, respectively, in Figs. 13(a)–13(f) versus the wave vector k_X/π. Again, the principal peaks in these transforms occur at $k_X = 0$ (or 2π); but, subsidiary peaks occur because of the shell structure imposed by the confining potential.
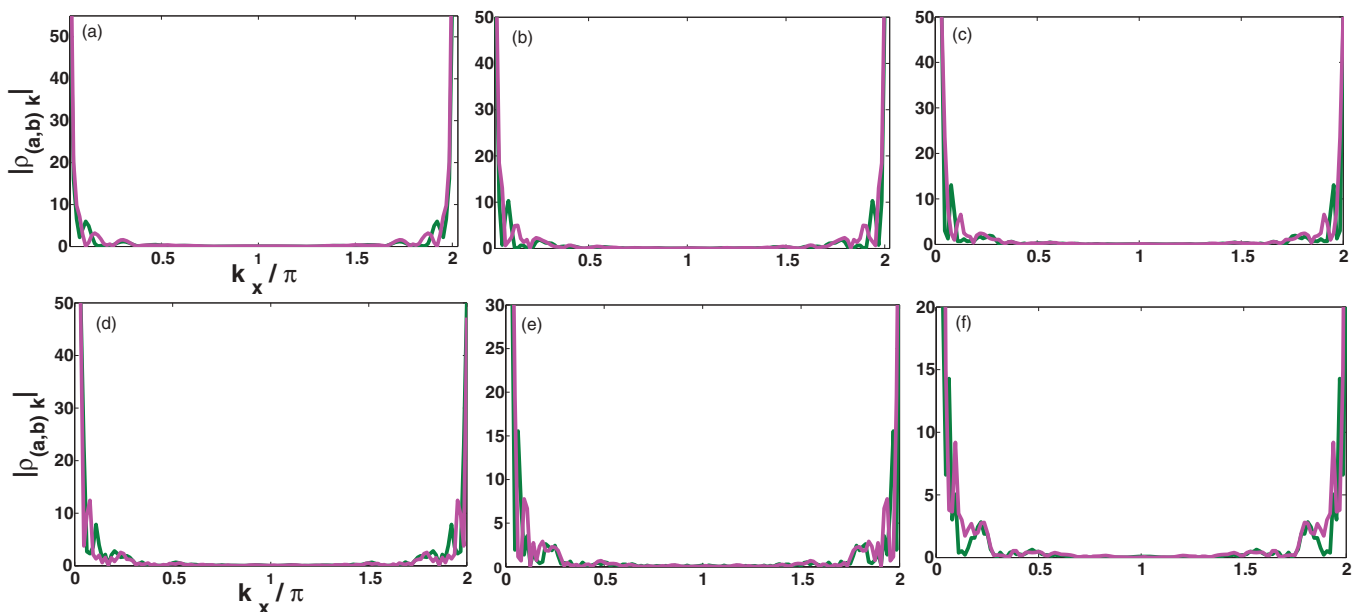

FIG. 11. (Color online) The moduli of the one-dimensional Fourier transforms, namely, $|\rho_{(a,b)k}|$, of the plots of $\rho_{(a,b)i}$ in Figs. 10(a)–10(f) are plotted, respectively, in (a)–(f) here versus the wave vector k_X/π.
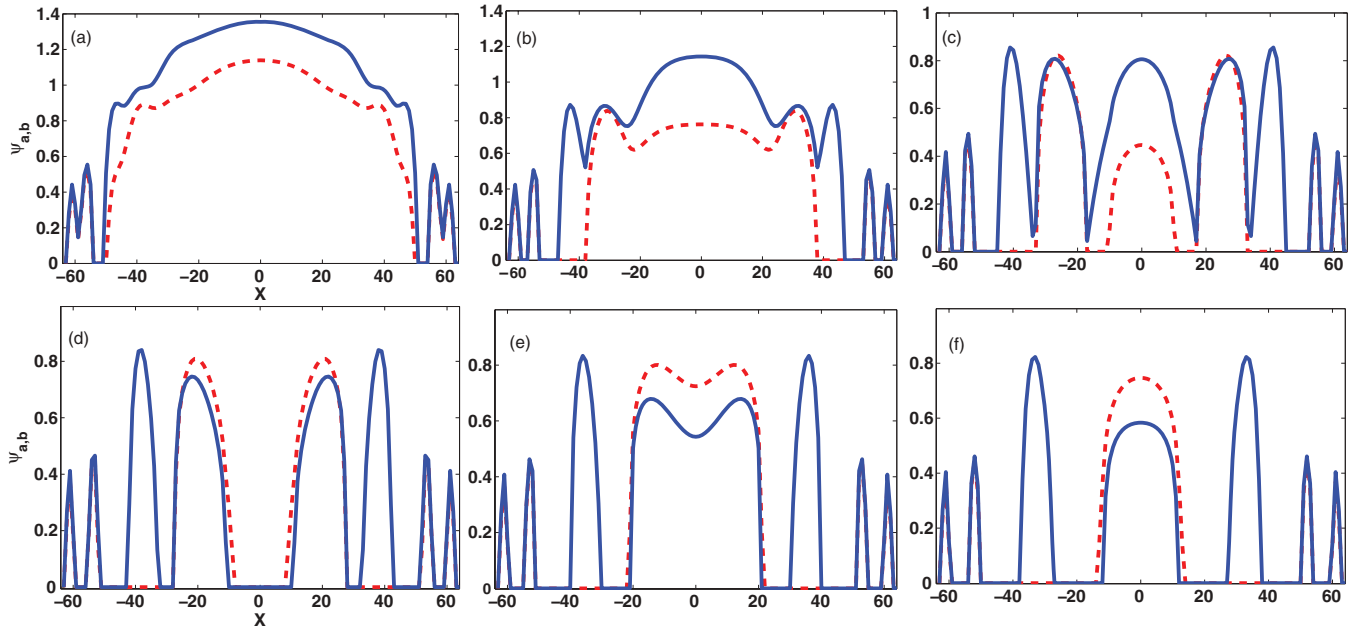
FIG. 12. (Color online) Plots of ψ_{ai} (red dashed line) and ψ_{bi} (blue line) versus X, along the $Y = Z = 0$ line, with $\mu_a = \mu_b = 30$, $V_T/(zt) = 0.008$, and (a) $U_a/(zt) = 8$, $U_b = 0.9U_a$, and $U_{ab} = 0.6U_a$, (b) $U_a/(zt) = 10$, $U_b = 0.9U_a$, and $U_{ab} = 0.6U_a$, (c) $U_a/(zt) = 11$, $U_b = 0.9U_a$, and $U_{ab} = 0.6U_a$, (d) $U_a/(zt) = 12$, $U_b = 0.9U_a$, and $U_{ab} = 0.6U_a$, (e) $U_a/(zt) = 13$, $U_b = 0.9U_a$, and $U_{ab} = 0.6U_a$, and (f) $U_a/(zt) = 14$, $U_b = 0.9U_a$, and $U_{ab} = 0.6U_a$.

In Figs. 14(a)–14(d), we show representative density and order-parameter profiles, for ρ_a and ψ_a, and the moduli of their one-dimensional Fourier transforms (see paragraph above) for $U_{ab} = 2.22U_a$, $U_b = 0.65U_a$, $U_a = 13$, $\mu_b = 0.8\mu_a$, $V_T = 0.008$, and $L = 64$. With this set of parameter values, ρ_b and ψ_b vanish.

The density and order-parameter profiles of Figs. 10 and 12 lead to the shell structure that we describe below. For

specificity, consider Figs. 10(d) and 12(d). These plots show that, along the line $Y = Z = 0$, in the region from $X = 0$ to $|X| \equiv 10$ the system has an MI phase for both types of bosons with $\rho_b = \rho_a = 2$ and $\psi_a = \psi_b = 0$; in the regions $10 < X < 28$ and $-28 < X < -10$, the system displays an SF phase for both types of bosons with $\rho_b > \rho_a$ and slightly $\psi_a > \psi_b > 0$; in the intervals $28 < X < 50$ and $-50 < X < -28$ bosons of type a are in an MI phase with $\rho_a = 1$; when $28 < X < 34$
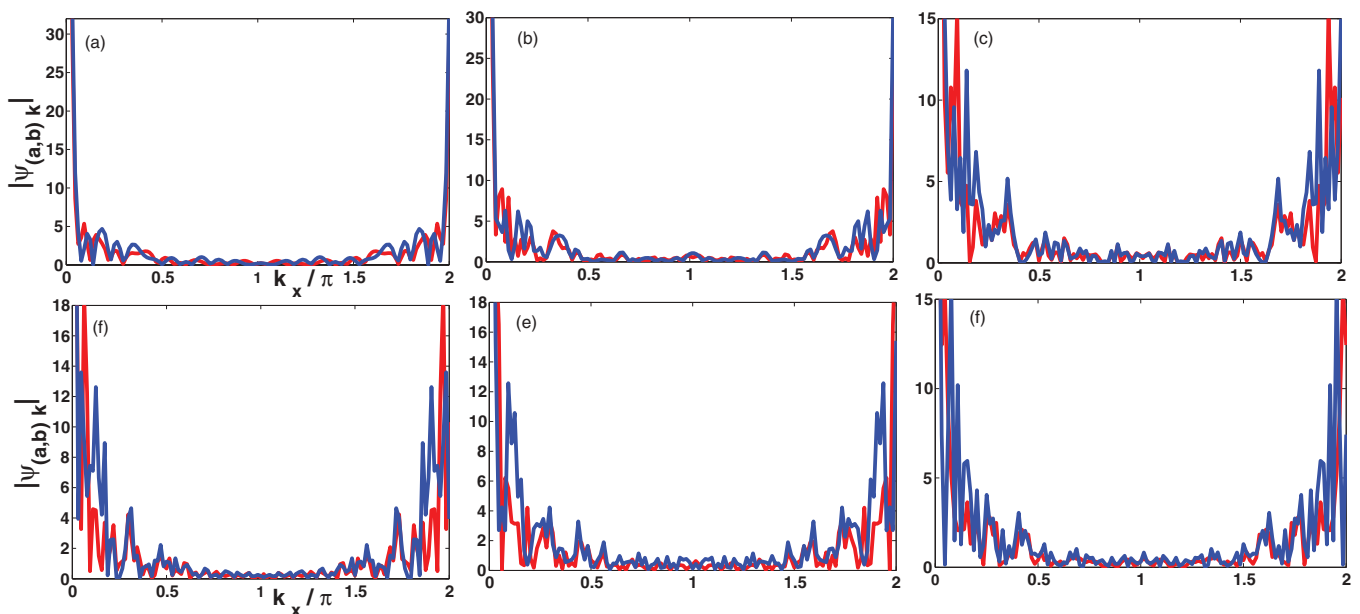

FIG. 13. (Color online) The moduli of the one-dimensional Fourier transforms, namely, $|\psi_{(a,b)k}|$, of the plots of $\psi_{(a,b)i}$ in Figs. 12(a)–12(f) are plotted, respectively, in (a)–(f) here versus the wave vector k_X/π.
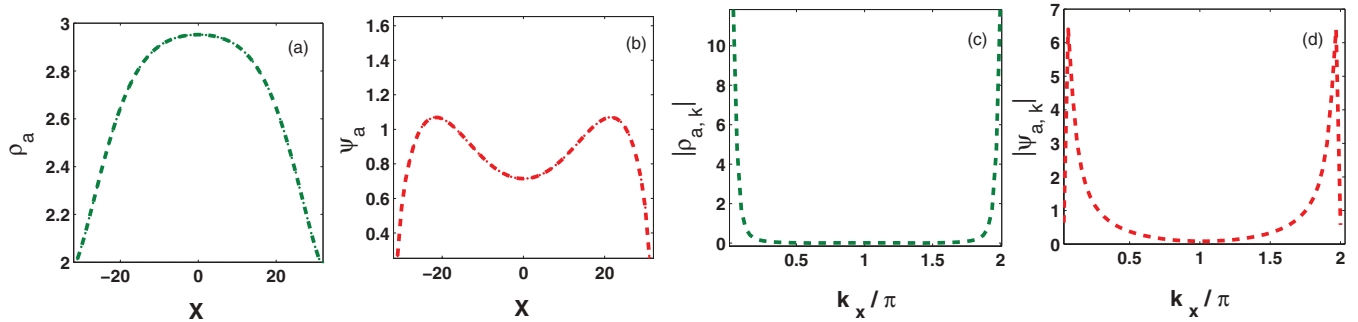
FIG. 14. (Color online) Plots of (a) $\rho_{a,i}$ and (b) $\psi_{a,i}$ versus X, along the $Y = Z = 0$ line, with $U_{ab} = 2.22U_a$, $U_b = 0.65U_a$, $U_a = 13$, $\mu_b = 0.8\mu_a$, $V_T = 0.008$, and $L = 64$ (with this set of parameter values, ρ_b and ψ_b vanish); corresponding plots of the moduli of the one-dimensional Fourier transforms, namely, (c) $|\rho_{a,k}|$, and (d) $|\psi_{a,k}|$ versus the wave vector k_X are also shown here.

or $-34 < X < -28$ bosons of type b are in an MI phase with $\rho_b = 2$; in the regions $34 < X < 42$ and $-42 < X < -34$ bosons of type b are in an SF phase whereas those of type a are still in the MI phase with $\rho_a = 1$; if $42 < X < 50$ or $-50 < X < -42$, then we have an MI phase for both types of bosons with $\rho_b = \rho_a = 1$; at slightly larger values of $|X|$, the system moves into an SF phase with $\rho_a = \rho_b > 0$ and $\psi_a = \psi_b > 0$; at even larger values of $|X|$, the system moves into a very narrow MI phase for both types of bosons with $\rho_a = \rho_b = 0.5$, such that the total density for the system is $\rho = \rho_a + \rho_b = 1$ and $\psi_a = \psi_b = 0$; as $|X|$ increases further, the system displays a very narrow SF region until it enters a

small region in which the boson density vanishes for the both types of bosons.

From the profiles in Figs. 10, and 12(a)–12(f), it is clear that the precise sequence and types of MI and SF shells depend on the parameters in the BH model (3) for two species of bosons. These SF and MI shells appear as annuli in a 2D planar section $\mathcal{P}_Z$ through the 3D lattice, at a vertical distance Z from the center as shown, for $\mathcal{P}_{Z=0}$, in Figs. 15(a) and 15(b), for bosons of types a and b, respectively, for the profiles of Figs. 10(d) and 12(d). Similar annular structures for the profiles of Figs. 10(e) and 12(e) are given in Figs. 15(c) and 15(d). We do not display the annular structures for the other profiles in Figs. 10 and 12.
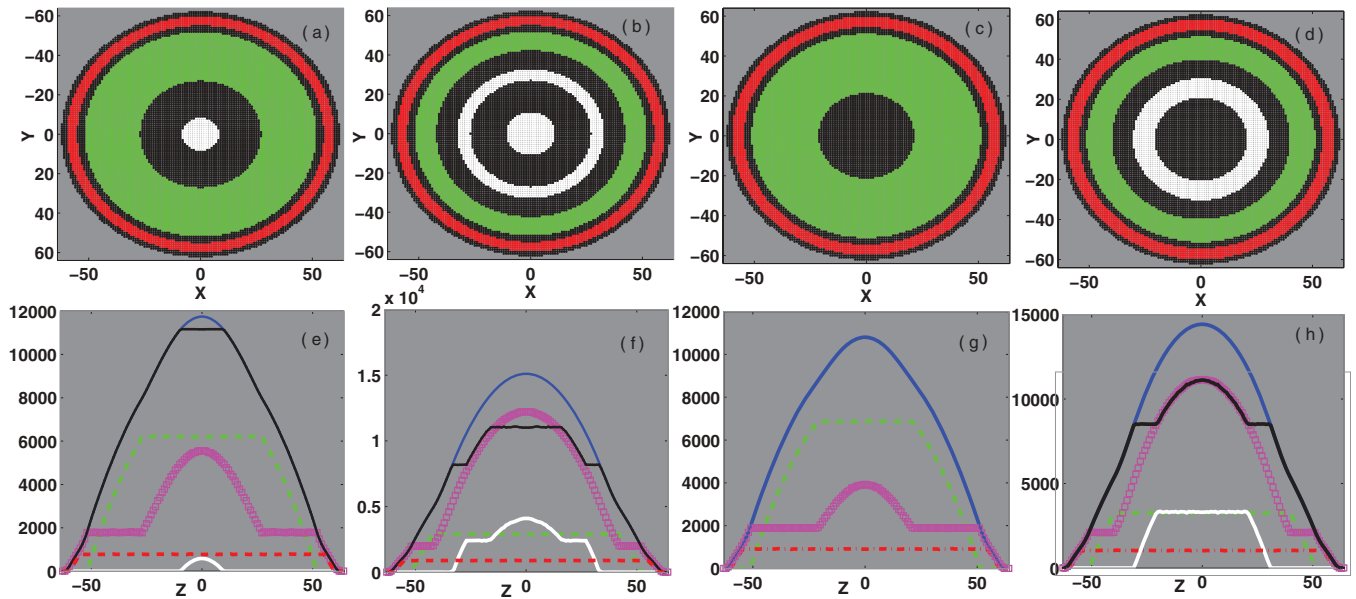

FIG. 15. (Color online) SF (black), MI2 (white), MI1 (green), MI(a,b) 1/2 (red) annuli in the 2D planar section $\mathcal{P}_{Z=0}$ (see text) with $U_a/(zt) = 12$, $U_b = 0.9U_a$, $U_{ab} = 0.6U_a$, $V_T/(zt) = 0.008$, and $\mu_a = \mu_b = 30$ for bosons of (a) type a and (b) type b; for these parameter values, the integrated, in-trap density profiles are plotted versus Z in (e) and (f), respectively. These in-trap profiles show the total number of bosons for types a and b; N_{a_T}, N_{b_T} (blue full lines), the number of bosons in MI2 and MI1 regions, N_{a_2}, N_{b_2} [white lines in (e) and (f)] and N_{a_1}, N_{b_1} [green dashed lines in (e) and (f)], respectively, the numbers of bosons in MI(a,b) 1/2 [red dashed lines in (e) and (f)] regions, $[N_{a_T} - N_{a_2}, N_{b_T} - N_{b_2}]$ [black full line in (e) and (f)], and $[N_{a_T} - N_{a_1}, N_{b_T} - N_{b_1}]$ [pink annuli in (e) and (f)]. The annular structures for the profiles of Figs. 10(e) and 12(e) are given in (c) and (d) and the corresponding integrated, in-trap density profiles in (g) and (h), respectively. The outermost gray regions in (a)–(d) contain no bosons.

in Figs. 15(e) and 15(f)], respectively, the numbers of bosons in $MI_{(a,b)}$ 1/2 [red dashed lines in Figs. 15(e) and 15(f)] regions, $[N_{a_T} - N_{a_2}, N_{b_T} - N_{b_2}]$ [black full lines in Figs. 15(e) and 15(f)], and $[N_{a_T} - N_{a_1}, N_{b_T} - N_{b_1}]$ (pink annuli) in Figs. 15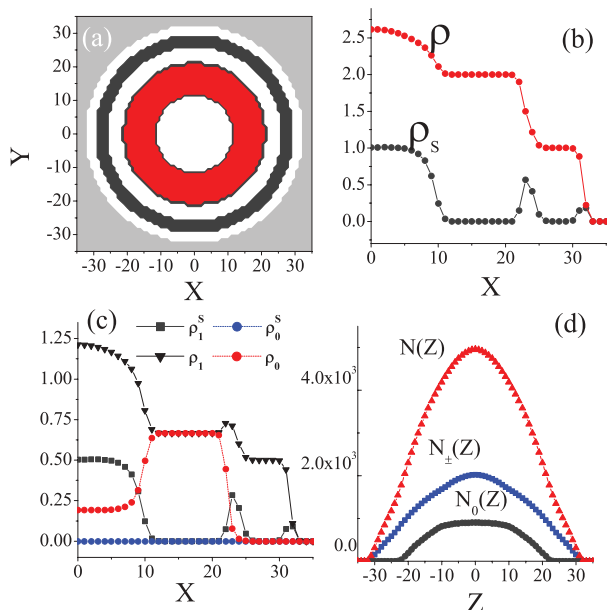(e) and 15(f). The outermost gray regions contain no bosons. Integrated, in-trap density profiles for the planar sections in Figs. 15(c) and 15(d) are shown in Figs. 15(g) and 15(h), respectively.

C. Results for the spin-1 Bose-Hubbard model

With the order parameters that we have defined in Eq. (10), we can obtain phase diagrams for the spin-1 BH model for various values of U_0 and U_2; we refer the reader to our earlier study[22] for such phase diagrams that include polar and ferromagnetic SF phases. Here, we use the inhomogeneous MF theory, which we have developed above for the spin-1 BH model, to obtain some illustrative results for order-parameter profiles in a representative case that has a polar superfluid. In particular, we consider a simple-cubic lattice with 70^3 sites, $\mu/E_r = 1$, $V_T/E_r = 0.001$, $V_0/E_r = 14.5$, and $U_2/U_0 = 0.03$. The 2D planar section $\mathcal{P}_Z$ for $Z = 0$ is plotted in Fig. 16(a). The radial variations of the total onsite density of bosons $\rho_i = \sum_\sigma \rho_{i,\sigma}$ and total onsite superfluid density $\rho_i^s = \sum_\sigma \rho_{i,\sigma}^s = \sum_\sigma |\psi_{i,\sigma}|^2$, as well as the individual component of superfluid density $|\psi_{i,\sigma}|^2$, are given in Figs. 16(b) and 16(c), respectively. From Fig. 16(b) it is evident that this system has two well-developed MI ($\rho = 1$ and 2) shells, which are represented as black and red regions, respectively. The most important result for model (3) (Ref. 22) is that the superfluid phase is polar for $U_2 > 0$ and, within our MF theory, the superfluid order parameters take one of the two possible sets of values; $\psi_{\pm 1} \neq 0$, $\psi_0 = 0$ or $\psi_{\pm 1} = 0$, $\psi_0 \neq 0$. Figure 16(c) yields $\psi_{\pm} 1 > 0$ and $\psi_0 = 0$ in the superfluid phase, thus confirming the polar nature of the phase. Another important feature is that $\rho_{i,\pm 1} \neq \rho_{i,0}$ in the polar superfluid phase. This leads to $N_{\pm 1}(Z) \neq N_0(Z)$, where $N_\sigma(Z)$ is the total number of bosons with a spin σ in the 2D planar section $\mathcal{P}_Z$ and is plotted in Fig. 16(d) versus Z. Thus, the determination of $N_\sigma(Z)$ experimentally can reveal these features and can be used to confirm the polar nature of the superfluid phase in a system of spin-1 bosons in an optical lattice.

FIG. 16. (Color online) (a) SF (white) and MI regions [$\rho = 2$ (red) and $\rho = 1$ (black)] annuli formed in the 2D section though the 3D optical lattice at the center and (b) the corresponding radial variation of density ρ_i and superfluid density ρ_i^s; (c) radial variation of $\rho_{i\sigma}$ and $\rho_{i,\sigma}^s$ and (d) $N_\sigma(Z)$ versus Z for $\sigma = \pm 1,0$. Note that $N_{-1}(Z) = N_1(Z)$. $N(Z) = \sum_\sigma N_\sigma$. Here, the optical-lattice parameters are taken to be $\mu/E_r = 1$, $V_T/E_r = 0.001$, $V_0/E_r = 14.5$, and $U_2/U_0 = 0.03$.

For any 2D planar section $\mathcal{P}_Z$, we can calculate integrated, in-trap density profiles such as $N_m(Z)$, the number of bosons in the $\rho = m$ MI annulus, as we have discussed for the BH model with one species of bosons. Here, m is an integer; we concentrate on $m = 1$ or 2. We can also calculate the remaining number of bosons, e.g., $N_{am}^r(Z) = N_{aT} - N_{am}(Z)$ or $N_{bm}^r(Z) = N_{bT} - N_{bm}(Z)$. For the parameter values of Figs. 15(a) and 15(b), illustrative integrated, in-trap density profiles are plotted versus Z in Figs. 15(e) and 15(f), respectively. These in-trap profiles show the total number of bosons for type a and b, N_{aT} and N_{bT} (blue full lines), the number of bosons in MI2 and MI1 regions, N_{a_2}, N_{b_2} [white lines in Figs. 15(e) and 15(f)] and N_{a_1}, N_{b_1} (green dashed lines
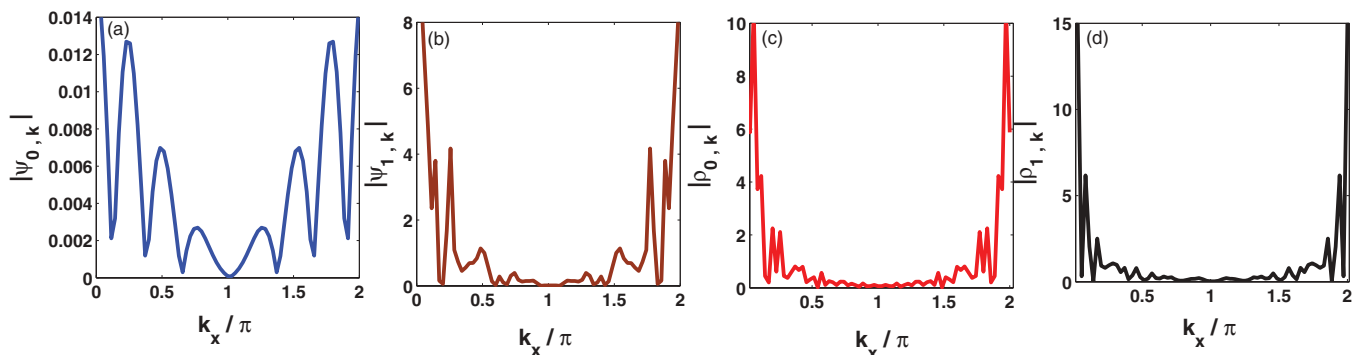

FIG. 17. (Color online) Illustrative plots of the moduli of the one-dimensional Fourier transforms (a) $|\psi_{0,k}|$, (b) $|\psi_{1,k}|$, (c) $|\rho_{0,k}|$, and (d) $|\rho_{1,k}|$ for the profiles in Fig. 16(c).
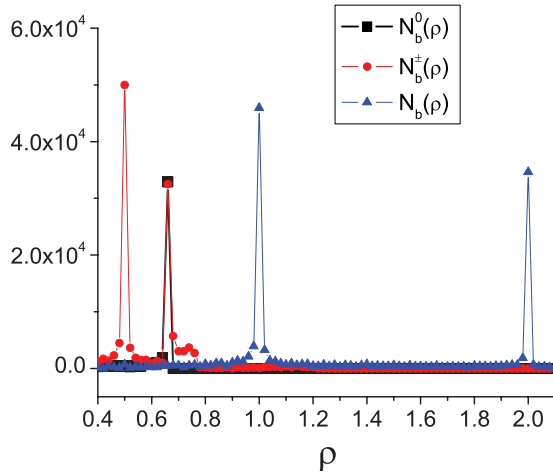
FIG. 18. (Color online) Representative plots versus the density ρ of $N_b^\pm(\rho)$ (red circles), the total number of bosons, at density ρ and with $\sigma = \pm 1$, $N_b^0(\rho)$ (black squares), the total number of bosons, at density ρ and with $\sigma = 0$, and their sum $N_b(\rho) = N_b^+(\rho) + N_b^0(\rho) + N_b^-(\rho)$ (blue triangles); here, all parameters are as in Fig. 16.

In Fig. 17, we show moduli of the one-dimensional Fourier transforms of the density and order-parameter profiles in Fig. 16(c). It would be interesting to see if such patterns can be obtained via time-of-flight measurements.

In Fig. 18, we show a representative plot of the analog of Fig. 6 for the spin-1 BH model with parameter values as in Fig. 16; thus, there are two well-developed MI shells. Here, $N_b^\pm(\rho)$ denotes the total number of bosons, at density ρ, and with $\sigma = \pm 1$; similarly, $N_b^0(\rho)$ is the total number of bosons, at density ρ, and with $\sigma = 0$; and $N_b(\rho)$ is the total number of bosons at density ρ. For the peak in $N_b(\rho)$, in the vicinity of $\rho = 1$, only bosons with $\sigma = \pm 1$ contribute; but, for the one near $\rho = 2$, all three components contribute equally. This result, which is also implicit in Fig. 16(c), should be verifiable in atomic-clock-shift experiments of the type that have been carried out for spinless bosons.[27]

We have noted in earlier work[22] that our mean-field theory does not account for order parameters that distinguish between different spin orderings, which have been studied[37] in the limit $U_0 \to \infty$, in the MI phases in spin-1 BH models. The exploration of such orderings lies beyond the scope of this study.

IV. CONCLUSIONS

We have carried out a comprehensive study of Mott insulator and superfluid shells in Bose-Hubbard models for bosons in optical lattices with harmonic traps by using an intuitively appealing inhomogeneous mean-field theory that has been used earlier to understand the Bose-glass phase.[23] Our inhomogeneous mean-field theory agrees quantitatively with QMC simulations in 2D. However, a naive application of our mean-field theory, with a single-site Hamiltonian, can not obtain the checkerboard state seen in Ref. 17 for a Bose-Hubbard model with two species of bosons and onsite interactions treated at the hard-core level. To obtain such a checkerboard state, we must allow for a doubled unit cell

(see, e.g., our study of the extended Bose-Hubbard model in Ref. 38); a detailed calculation of this checkerboard state lies beyond the scope of our paper here.

The inhomogeneous mean-field theory is numerically less intensive than QMC simulations; thus, we are able to perform calculation on experimentally realistic, large 3D systems and explore a wide range of parameter values. We can calculate in-trap density profiles that agree qualitatively with experiments,[26] and we show how to obtain the phase diagram of the homogeneous Bose-Hubbard model from such in-trap density profiles. Our results are also of direct relevance to recent atomic-clock-shift experiments[27] as we have described above. Finally, we have generalized our inhomogeneous mean-field theory to BH models with two species of bosons and a spin-1 BH model with harmonic traps. With two species of bosons, we obtain rich phase diagrams that have a variety of SF and MI phases and associated shells, when we include a quadratic confining potential; we also obtain in-trap density distributions that show plateaux as in the single-species case. For the spin-1 BH model, we show, in a representative case, that the system can display alternating shells of polar SF and MI phases,[22] and we make interesting predictions for atomic-clock-shift experiments. We hope our results will stimulate more experiments on such systems of bosons in optical lattices. Our inhomogeneous mean-field theory can also be applied to study the extended Bose-Hubbard model as we report elsewhere.[38]

Although other groups[29–34] have studied such shell structure theoretically, they have not obtained the quantitative agreement with quantum Monte Carlo (QMC) simulations[24] that we obtain, except in one dimension.[35] Furthermore, there have been some investigations of the BH model with a harmonic trap potential; these use mean-field theory[13,33] and, in addition, a local density approximation (LDA), which assumes that the properties of a system with finite confining potential at a particular location are identical to those of a uniform system with the value of the local chemical potential at that location. This approximation leads to a decoupling of each site from its neighbor; it is equivalent to assuming $\phi_i = \psi_i$ in Eq. (5) and a minimization of the ground-state energy for each site separately. In our inhomogeneous mean-field theory, we do not make this additional LDA assumption, and the minimization of the ground-state energy is done over the entire set of ψ_i. If we compare these two approaches for the single-species BH model, we find that the difference is negligible in SF regions, but discrepancies exist at SF-MI interfaces; this has been reported in other models[39] also. A Gutzwiller-type approximation has been used recently[40] to study the Bose-glass phase in the spin-1 BH model. In a recent study,[41] an inhomogeneous mean-field theory like ours is used as a starting point for the generalization of a strong-coupling expansion[42] to the Bose-Hubbard model.

*rvpai@unigoa.ac.in

†jamshid@physics.iisc.ernet.in

‡kshesh@gmail.com

§Also at Jawaharlal Nehru Centre For Advanced Scientific Research, Jakkur, Bangalore, India; rahul@physics.iisc.ernet.in

[1] I. Bloch, J. Dalibard, and W. Zwerger, Rev. Mod. Phys. **80**, 885 (2008); M. Lewenstein *et al*., Adv. Phys. **56**, 243 (2007).

[2] D. Jaksch, C. Bruder, J. I. Cirac, C. W. Gardiner, and P. Zoller, Phys. Rev. Lett. **81**, 3108 (1998).

[3] M. Greiner *et al*., Nature (London) **415**, 39 (2002).

[4] M. P. A. Fisher, P. B. Weichman, G. Grinstein, and D. S. Fisher, Phys. Rev. B **40**, 546 (1989); D. S. Rokhsar and B. G. Kotliar, *ibid*. **44**, 10328 (1991); W. Krauth, M. Caffarel, and J. P. Bouchaud, *ibid*. **45**, 3137 (1992).

[5] K. Sheshadri *et al*., Europhys. Lett. **22**, 257 (1993).

[6] W. Krauth, N. Trivedi, and D. Ceperley, Phys. Rev. Lett. **67**, 2307 (1991); N. Trivedi and M. Makivic, *ibid*. **74**, 1039 (1995).

[7] J. Catani, L. DeSarlo, G. Barontini, F. Minardi, and M. Inguscio, Phys. Rev. A **77**, 011603(R) (2008).

[8] S. Trotzky *et al*., Science **319**, 295 (2008).

[9] A. B. Kuklov and B. V. Svistunov, Phys. Rev. Lett. **90**, 100401 (2003).

[10] J.-R. Han, Phys. Lett. A **332**, 131 (2004).

[11] P. Buonsante, S. M. Giampaolo, F. Illuminati, V. Penna, and A. Vezzani, Phys. Rev. Lett. **100**, 240402 (2008).

[12] A. Hu, L. Mathey, I. Danshita, E. Tiesinga, C. J. Williams, and C. W. Clark, Phys. Rev. A **80**, 023619 (2009).

[13] T. Ozaki and T. Nikuni, J. Phys.: Conf. Ser. **150**, 042158 (2009).

[14] G. H. Chen and Y. S. Wu, Phys. Rev. A **67**, 013606 (2003).

[15] A. Isacsson, M.-C. Cha, K. Sengupta, and S. M. Girvin, Phys. Rev. B **72**, 184507 (2005).

[16] T. Roscilde and J. I. Cirac, Phys. Rev. Lett. **98**, 190402 (2007).

[17] M. Guglielmino, V. Penna, and B. Capogrosso-Sansone, Phys. Rev. A **82**, 021601(R) (2010); **84**, 031603(R) (2011).

[18] Y. Li, M. R. Bakhtiari, L. He, and W. Hofstetter, Phys. Rev. A **85**, 023624 (2012).

[19] See, e.g., H.-J. Miesner, J. Stenger, S. Inouye, A. P. Chikkatur, and W. Ketterle, Phys. Rev. Lett. **82**, 2228 (1999).

[20] T. L. Ho, Phys. Rev. Lett. **81**, 742 (1998).

[21] S. Mukerjee, C. Xu, and J. E. Moore, Phys. Rev. Lett. **97**, 120406 (2006).

[22] R. V. Pai, K. Sheshadri, and R. Pandit, Phys. Rev. B **77**, 014503 (2008), and references therein.

[23] K. Sheshadri, H. R. Krishnamurthy, R. Pandit, and T. V. Ramakrishnan, Phys. Rev. Lett. **75**, 4075 (1995).

[24] S. Wessel, F. Alet, M. Troyer, and G. G. Batrouni, Phys. Rev. A **70**, 053615 (2004).

[25] V. A. Kashurnikov, N. V. Prokofev, and B. V. Svistunov, Phys. Rev. A **66**, 031601 (2002).

[26] S. Fölling, A. Widera, T. Muller, F. Gerbier, and I. Bloch, Phys. Rev. Lett. **97**, 060403 (2006).

[27] G. K. Campbell *et al*., Science **313**, 649 (2006).

[28] Stefan S. Natu, David C. McKay, Brian DeMarco, and Erich J. Mueller, Phys. Rev. A **85**, 061601 (2012).

[29] S. Bergkvist, P. Henelius, and A. Rosengren, Phys. Rev. A **70**, 053601 (2004).

[30] L. Pollet, S. Rombouts, K. Heyde, and J. Dukeksky, Phys. Rev. A **69**, 043601 (2004).

[31] B. DeMarco, C. Lannert, S. Vishveshwara, and T. C. Wei, Phys. Rev. A **71**, 063601 (2005).

[32] K. Mitra, C. J. Williams, and C. A. R. Sá de Melo, Phys. Rev. A **77**, 033607 (2008).

[33] I. B. Spielman, W. D. Phillips, and J. V. Porto, Phys. Rev. Lett. **98**, 080404 (2007); **100**, 120402 (2008).

[34] Y. Kato, Q. Zhou, N. Kawashima, and N. Trivedi, Nat. Phys. **4**, 617 (2008).

[35] G. G. Batrouni, H. R. Krishnamurthy, K. W. Mahmud, V. G. Rousseau, and R. T. Scalettar, Phys. Rev. A **78**, 023627 (2008).

[36] C. K. Law, H. Pu, and N. P. Bigelow, Phys. Rev. Lett. **81**, 5257 (1998).

[37] J. Arlt, K. Dholakia, J. Soneson, and E. M. Wright, Phys. Rev. A **63**, 063602 (2001); G. Fáth and J. Sólyom, Phys. Rev. B **51**, 3620 (1995).

[38] J. M. Kurdestany, R. V. Pai, and R. Pandit, Ann. Phys. (Berlin) **524**, 234 (2012).

[39] S. M. Pittman, G. G. Batrouni, and R. T. Scalettar, Phys. Rev. B **78**, 214208 (2008).

[40] M. Lkacki, S. Paganelli, V. Ahufinger, A. Sanpera, and J. Zakrzewski, Phys. Rev. A **83**, 013605 (2011).

[41] M. Gupta, H. R. Krishnamurthy, and J. K. Freericks (unpublished).

[42] J. K. Freericks, H. R. Krishnamurthy, Y. Kato, N. Kawashima, and N. Trivedi, Phys. Rev. A **79**, 053631 (2009).